*Final Report*

FDOT Contract No.: BDK75 977-66
UF Contract No.: 00100976

# Detection of Sinkholes or Anomalies Using Full Seismic Wave Fields


Principal Investigator: Michael McVay, Ph.D.
University of Florida
Engineering School of Sustainable Infrastructure and Environment
Department of Civil and Coastal Engineering
P.O. Box 116580
Gainesville, FL 32611-6580

Principal Researcher: Khiem T. Tran, Ph.D.
Clarkson University
Department of Civil and Environmental Engineering
Rowley Laboratories
Potsdam, New York


Developed for the


Project Manager: David Horhota, P.E., Ph.D.

*May 2013*

## DISCLAIMER

"The opinions, findings, and conclusions expressed in this publication are those of the authors and not necessarily those of the State of Florida Department of Transportation or the U.S. Department of Transportation.

Prepared in cooperation with the State of Florida Department of Transportation and the U.S. Department of Transportation."

# SI (MODERN METRIC) CONVERSION FACTORS (from FHWA)

**APPROXIMATE CONVERSIONS TO SI UNITS**

| SYMBOL | WHEN YOU KNOW | MULTIPLY BY | TO FIND | SYMBOL |
|---|---|---|---|---|
| **LENGTH** | | | | |
| **in** | inches | 25.4 | millimeters | mm |
| **ft** | feet | 0.305 | meters | m |
| **yd** | yards | 0.914 | meters | m |
| **mi** | miles | 1.61 | kilometers | km |

| SYMBOL | WHEN YOU KNOW | MULTIPLY BY | TO FIND | SYMBOL |
|---|---|---|---|---|
| **AREA** | | | | |
| **$in^2$** | square inches | 645.2 | square millimeters | $mm^2$ |
| **$ft^2$** | square feet | 0.093 | square meters | $m^2$ |
| **$yd^2$** | square yard | 0.836 | square meters | $m^2$ |
| **ac** | acres | 0.405 | hectares | ha |
| **$mi^2$** | square miles | 2.59 | square kilometers | $km^2$ |

| SYMBOL | WHEN YOU KNOW | MULTIPLY BY | TO FIND | SYMBOL |
|---|---|---|---|---|
| **VOLUME** | | | | |
| **fl oz** | fluid ounces | 29.57 | milliliters | mL |
| **gal** | gallons | 3.785 | liters | L |
| **$ft^3$** | cubic feet | 0.028 | cubic meters | $m^3$ |
| **$yd^3$** | cubic yards | 0.765 | cubic meters | $m^3$ |
| NOTE: volumes greater than 1000 L shall be shown in $m^3$ | | | | |

| SYMBOL | WHEN YOU KNOW | MULTIPLY BY | TO FIND | SYMBOL |
|---|---|---|---|---|
| **MASS** | | | | |
| **oz** | ounces | 28.35 | grams | g |
| **lb** | pounds | 0.454 | kilograms | kg |
| **T** | short tons (2000 lb) | 0.907 | megagrams (or "metric ton") | Mg (or "t") |

| SYMBOL | WHEN YOU KNOW | MULTIPLY BY | TO FIND | SYMBOL |
|---|---|---|---|---|
| **TEMPERATURE (exact degrees)** | | | | |
| **$^oF$** | Fahrenheit | 5 (F-32)/9<br>or (F-32)/1.8 | Celsius | $^oC$ |

| SYMBOL | WHEN YOU KNOW | MULTIPLY BY | TO FIND | SYMBOL |
|---|---|---|---|---|
| **ILLUMINATION** | | | | |
| **fc** | foot-candles | 10.76 | lux | lx |
| **fl** | foot-Lamberts | 3.426 | candela/$m^2$ | $cd/m^2$ |

| SYMBOL | WHEN YOU KNOW | MULTIPLY BY | TO FIND | SYMBOL |
|---|---|---|---|---|
| **FORCE and PRESSURE or STRESS** | | | | |
| **lbf** | pound force | 4.45 | newtons | N |
| **$lbf/in^2$** | pound force per square inch | 6.89 | kilopascals | kPa |

**APPROXIMATE CONVERSIONS TO SI UNITS**

| SYMBOL | WHEN YOU KNOW | MULTIPLY BY | TO FIND | SYMBOL |
|---|---|---|---|---|
| | | **LENGTH** | | |
| **mm** | millimeters | 0.039 | inches | in |
| **m** | meters | 3.28 | feet | ft |
| **m** | meters | 1.09 | yards | yd |
| **km** | kilometers | 0.621 | miles | mi |

| SYMBOL | WHEN YOU KNOW | MULTIPLY BY | TO FIND | SYMBOL |
|---|---|---|---|---|
| | | **AREA** | | |
| **$mm^2$** | square millimeters | 0.0016 | square inches | $in^2$ |
| **$m^2$** | square meters | 10.764 | square feet | $ft^2$ |
| **$m^2$** | square meters | 1.195 | square yards | $yd^2$ |
| **ha** | hectares | 2.47 | acres | ac |
| **$km^2$** | square kilometers | 0.386 | square miles | $mi^2$ |

| SYMBOL | WHEN YOU KNOW | MULTIPLY BY | TO FIND | SYMBOL |
|---|---|---|---|---|
| | | **VOLUME** | | |
| **mL** | milliliters | 0.034 | fluid ounces | fl oz |
| **L** | liters | 0.264 | gallons | gal |
| **$m^3$** | cubic meters | 35.314 | cubic feet | $ft^3$ |
| **$m^3$** | cubic meters | 1.307 | cubic yards | $yd^3$ |

| SYMBOL | WHEN YOU KNOW | MULTIPLY BY | TO FIND | SYMBOL |
|---|---|---|---|---|
| | | **MASS** | | |
| **g** | grams | 0.035 | ounces | oz |
| **kg** | kilograms | 2.202 | pounds | lb |
| **Mg (or "t")** | megagrams (or "metric ton") | 1.103 | short tons (2000 lb) | T |

| SYMBOL | WHEN YOU KNOW | MULTIPLY BY | TO FIND | SYMBOL |
|---|---|---|---|---|
| | | **TEMPERATURE (exact degrees)** | | |
| **$^oC$** | Celsius | 1.8C+32 | Fahrenheit | $^oF$ |

| SYMBOL | WHEN YOU KNOW | MULTIPLY BY | TO FIND | SYMBOL |
|---|---|---|---|---|
| | | **ILLUMINATION** | | |
| **lx** | lux | 0.0929 | foot-candles | fc |
| **$cd/m^2$** | candela/$m^2$ | 0.2919 | foot-Lamberts | fl |

| SYMBOL | WHEN YOU KNOW | MULTIPLY BY | TO FIND | SYMBOL |
|---|---|---|---|---|
| | | **FORCE and PRESSURE or STRESS** | | |
| **N** | newtons | 0.225 | pound force | lbf |
| **kPa** | kilopascals | 0.145 | pound force per square inch | $lbf/in^2$ |

*SI is the symbol for International System of Units. Appropriate rounding should be made to comply with Section 4 of ASTM E380.
(Revised March 2003)

## TECHNICAL REPORT DOCUMENTATION PAGE

| 1. Report No. | 2. Government Accession No. | 3. Recipient's Catalog No. |
|---|---|---|
| | | |

| 4. Title and Subtitle | 5. Report Date |
|---|---|
| Detection of Sinkholes or Anomalies<br>Using Full Seismic Wave Fields | April 2013 |
| | 6. Performing Organization Code |
| 7. Author(s)<br>Michael McVay and Khiem T. Tran | 8. Performing Organization Report No. |
| 9. Performing Organization Name and Address<br>University of Florida – Dept. of Civil and Coastal Engineering<br>Engineering School of Sustainable Infrastructure & Environment<br>365 Weil Hall – P.O. Box 116580<br>Gainesville, FL 32611-6580 | 10. Work Unit No. (TRAIS) |
| | 11. Contract or Grant No.<br>BDK75 977-66 |
| 12. Sponsoring Agency Name and Address<br>Florida Department of Transportation<br>605 Suwannee Street, MS 30<br>Tallahassee, FL 32399 | 13. Type of Report and Period Covered<br>*Draft* Final Report<br>04/24/2012 – 05/31/2013 |
| | 14. Sponsoring Agency Code |

15. Supplementary Notes

16. Abstract

This research presents an application of two-dimensional (2-D) time-domain waveform tomography for detection of embedded sinkholes and anomalies. The measured seismic surface wave fields were inverted using a full waveform inversion (FWI) technique, based on a finite-difference solution of 2-D elastic wave equations and Gauss–Newton inversion method. The key advantage of this approach was the ability to generate all possible wave propagation modes of seismic wave fields (body waves and Rayleigh waves) that were then compared with measured surface data to infer complex subsurface properties. Both the pressure wave (P-wave) and shear wave (S-wave) velocities were inverted independently and simultaneously. The FWI was applied to two synthetic and four real experimental data sets. The synthetic inversion results showed that the inversion was capable of detecting layering (e.g., strong over weak), and anomalies; in addition, the initial input velocity profile for the inversion was straightforward (i.e., linearly increasing with depth). The developed FWI algorithm could run on raw collected data with a minimum manual effort (no picking of first-arrival travel times). The inversion results of real data sets showed that the waveform analysis was able to delineate: 1) an embedded concrete culvert; 2) extent of multiple existing sinkholes/chimneys; and 3) a complex profile with an embedded void (unknown at time of data collection) and highly variable bedrock both laterally and vertically. Independent invasive testing (standard penetration test, SPT, and cone penetration testing, CPT) was conducted to verify the seismic test results. Finally, for the cases presented, the 2-D full waveform inversion was found computationally practical, i.e., the results were achieved in 2-4 hours of computer time on a standard laptop computer.

| 17. Key Words | 18. Distribution Statement |
|---|---|
| Geophysical Testing, Full Waveform Inversion,<br>Sinkhole, Anomalies, Field Testing | No restrictions. |

| 19. Security Classif. (of this report) | 20. Security Classif. (of this page) | 21. No. of Pages | 22. Price |
|---|---|---|---|
| Unclassified | Unclassified | 65 | |

**Form DOT F 1700.7** (8-72) Reproduction of completed page authorized

# ACKNOWLEDGMENTS

The researchers would first like to thank the Florida Department of Transportation (FDOT) for the financial support to carry out this research as well as the guidance of the project manager for its successful outcome. In addition, this research could not have been completed without the aid of the State Materials Office (SMO) and District 5 personnel. SMO was instrumental in lending the researchers the geophysical testing equipment and performing SPT testing on the Newberry, Florida, site. District 5 engineers assisted the researchers in locating US-441 sinkhole and sharing the CPT test results on the site.

# EXECUTIVE SUMMARY

The purpose of this study was to develop and implement a two-dimensional (2-D) full waveform inversion (FWI) technique using seismic waves for detection of embedded sinkholes or anomalies. The developed FWI technique was based on a finite-difference solution of 2-D elastic wave equations in time domain. It also employed a Gauss–Newton method to invert the seismic full wave fields of near-surface velocity profiles by matching the observed and computed waveforms in the time domain. Virtual sources and reciprocal wave fields were used to calculate partial derivative wave fields (gradient matrix) to reduce the computer time. Observed and estimated wave fields were convolved with appropriate reference traces to remove the influence of source signatures, i.e., the inversion technique was independent of sources, or source signatures were not required to be measured during field testing.

The technique was successfully applied to several synthetic and real data sets for detection of embedded sinkholes/anomalies. Results from synthetic data sets showed the useful capability of the FWI in characterization of air-filled or water-filled embedded voids. Results from real data sets showed that the FWI well characterized various site conditions that included an embedded concrete culvert, low-velocity anomalies, open chimneys, and a naturally occurring embedded void.

The unique features of the developed FWI technique included: a) shear wave (S-wave) and pressure wave (P-wave) velocities inverted independently and simultaneously to improve the validation of the characterized profiles; and b) Poisson's ratio ($\mu$) was estimated from the P-wave and S-wave velocities for possible indications of soil types. For example, $\mu$ for sand or rock were expected to be lower than that of clay. Voids can be characterized with both shear wave velocity ($V_s$) and $\mu$ close to zero for those filled with air, and $V_s$ close to 0 and $\mu$ close to 0.5 for

those filled with water. Currently, there is no analysis method providing both S- and P-wave velocities simultaneously in engineering scales, as acquired seismic wave fields are often dominated by strong Rayleigh wave components. Traditional seismic wave methods only provide either S- or P-wave velocities since the methods use only portions of wave fields, e.g., the dispersion property of Rayleigh waves or travel times of P-waves. Soil types are often difficult to distinguish, as some types of sand and clay may have the same S-wave velocity, or soft rock and water may have the same P-wave velocity. Both soil stiffness and soil types can be obtained from inversion of full seismic wave fields. Thus, the work was a critical step toward the use of an effective non-destructive testing method (FWI) for site investigations in the design of foundations and other geotechnical structures.

TABLE OF CONTENTS

LIST OF FIGURES

# CHAPTER 1
# INTRODUCTION

## 1.1 Background

Sinkholes have made headlines in many states throughout the United States (e.g., Florida, New Jersey, Tennessee, Kentucky, and California), as well as in South America, Europe, and Asia. Sinkholes can cause infrastructure damage and even collapse, which has resulted in serious economic impact and even loss of life (e.g., Tampa). The magnitude of the financial losses in Florida has been recently documented in a Florida Senate Banking and Insurance Committee (Jan. 2011) report; "Total claims in Florida have increased from 2,360 in 2006 to 6,694 in 2010, totaling 24,671 claims throughout that period.…Total sinkhole claim costs amounted to $**1.4 billion** during the 5-year time frame." Pre-construction detection of sinkholes or investigation of surface subsidence prior to large movements could substantially reduce this cost.

Sinkhole detection on a site usually begins with a non-destructive testing (NDT) study, as it provides a two-dimensional (2-D), depth × length view of subsurface conditions. At suspicious locations (anomalies), more involved invasive methods (one-dimensional (1-D) investigation), such as a cone penetration test (CPT) or standard penetration test (SPT), are performed to characterize the anomalies, if necessary. Since the 1980s, various NDT methods have been used to characterize sinkholes, including gravity, resistivity, and ground penetrating radar (GPR), and traditional seismic wave methods (Wightman et al., 2003). However, many existing methods have limitations in identifying and quantifying sinkholes.

For instance, gravity methods (LaFehr, 1980; Paterson and Reeves, 1985; Hansen, 2001) are capable of measuring small spatial differences in the gravitational pull of the earth. If the

void is close enough to the ground surface, then a reduction in the gravitational pull across the void can be measured, and the void may be located. However, if the void is embedded at a depth larger than the size of the void, the acquired data become insensitive to the void (Wightman et al., 2003), and will not be detected with any accuracy. Similarly, if the void is filled with water, the difference in gravity between soil and water is small compared to soil and air, limiting the detection of voids, especially with depth.

Resistivity methods (Loke, 2000a; 2000b) have also been employed to locate voids, since an air-filled void usually presents a strong electrical resistivity contrast with the host rock. However, the approach is only suited for finding shallow voids. In the case of deeper voids, longer electrode arrays are needed and such arrays are influenced by the large volume of overburden and rock scanned versus the fixed volume of the void (i.e., relatively small) making detection difficult (Wightman et al., 2003).

Ground penetrating radar (GPR) (Conyers and Goodman, 1997; Bristow and Jol, 2003; Daniels, 2004; and Jol, 2009) has been widely used to locate shallow cavities. GPR differentiation depends on having contrast in the dielectric properties of the target compared to the host overburden along with sufficient depth penetration to reach the target. Penetration of the GPR signal is severely limited in water saturated, electrically conductive ground containing clay (Slob et al., 2010). Moreover, GPR provides no credible information of material below the ground water level, and thus a void may not be detected if it is filled with water.

Seismic methods, including refraction tomography and Rayleigh wave approaches, have also been employed in locating voids (Wightman et al., 2003; Sheehan et al., 2005). However, the main limitation of existing seismic methods is that a small percentage of the waveform is actually used for detection and their sensitivity to voids is limited. For example, refraction

methods use only first-arrival signals to infer unknown material properties. The travel time from a source to a receiver is measured from the fastest ray that starts from the source and travels through a medium to the receiver. The fastest ray tends to go through stiffer (faster) material, and generally travels within a few meters at the top of the stiff layer (bedrock) regardless of the geophone spread (Tran and Hiltunen, 2012a). The technique fails to characterize the deeper material, and thus misses the embedded void in the bedrock. Similarly, Rayleigh wave approaches include techniques involving wave velocity dispersion, such as spectral analysis of surface waves (SASW) (Nazarian, 1984), multi-channel analysis of surface waves (MASW) (Park et al., 1999), and refraction microtremor (ReMi) (Louie, 2001). The dispersion property is developed by averaging the properties of whole volume of material within a depth of approximately one wavelength for each frequency. When the depth of investigation increases, lower frequency or longer wavelength components are required, resulting in larger volumes of material being utilized to derive the dispersion property. Consequently, the dispersion data becomes insensitive to the embedded void and its presence is difficult to discern.

As identified by Plessix (2008), and Virieux and Operto (2009), the full waveform inversion (FWI) approach offers the potential to produce higher resolution of the subsurface than the other approaches by extracting information contained in the complete waveforms rather than using only the dispersion property of Rayleigh waves or first-arrival signals. Nasseri–Moghaddama et al. (2007), for example, have clearly shown that the recorded responses at the surface can carry valuable information regarding the presence and characterization of anomalies, e.g., voids, below the surface. However, FWI is computationally intensive, requiring a full solution of the governing wave equations. Many algorithms for waveform inversion have been developed and applied to synthetic and real seismic data in large-scale (kilometer-scale) domains

(Shipp and Singh, 2002; Ravaut et al., 2004; Sheen et al., 2006; Cheong et al., 2006; Brenders and Pratt, 2007; and Choi and Alkhalifah, 2011). In the large-scale, surface waves are easily separated from body waves and are generally removed from the inversion process. However, at a shorter length scale (0–100 m), it is difficult to separate body waves from surface waves, and only a few studies of waveform inversion involving both body and surface waves have been performed for near-surface investigations on synthetic data (Gélis et al., 2007; and Romdhane et al., 2011).

Herein, an FWI technique was developed to invert both body and surface waves in the case of real experimental data. The technique employed a Gauss–Newton technique to invert the seismic full wave fields of near-surface velocity profiles by matching the observed and computed waveforms in the time domain. Virtual sources and a reciprocity principle were used to calculate partial derivative wave fields (gradient matrix) to reduce the computer time. Observed and estimated wave fields were convolved with appropriate reference traces to remove the influence of source signatures, i.e., the inversion technique was independent of sources, or source signatures were not required to be measured during field testing. The technique was successfully applied to several synthetic and real data sets for detection of embedded sinkholes/anomalies.

### 1.2 Objectives and Supporting Tasks

For possible application, the technology needed to be validated under a variety of real scenarios with sinkholes. The objective of this project was to show proof of the concept of using FWI for detection of sinkholes. For instance, sites identified as having a sinkhole were investigated through evasive means. The latter required standard penetration (i.e., borehole) or cone penetration testing. In addition, field testing required identifying the appropriate frequency

range of input energy excitation (i.e., size of hammer), geophone layout, etc. The work was accomplished systematically through the tasks listed below.

### 1.2.1 Task 1 – Development of a Test System with Laboratory Synthetic Models

The goal of this task was to develop a test system (hardware and software) for investigating sinkholes. The investigation focused on identifying both the active sources for generating the wave fields and the sensors to measure generated wave fields, as well as the properties of the active sources and test configurations. Specifically, an active source could only generate a wave field in a limited band of frequencies. However from preliminary analysis, it was found that both low frequency components (large wavelengths) for deep investigation of subsurface profiles and high frequency components (small wavelengths) for detection of small voids were required. The optimal ranges of frequencies were developed for each selection of equipment (for example, size of sledgehammers, dropped weights, or air guns) for the active sources.

Next, a number of parametric studies were performed with synthetic models. These model studies aided in developing sensor layout, as well as location/number of excitations (i.e., hammer blows). The work focused on source configurations to optimize both field testing and data analysis efforts. Using typical models for different types of sinkholes as starting points (different sizes, embedded depths, layering and layer thickness), wave fields were computed for alternative source and sensor configurations. By examining the inversions of synthetic wave field data, resolution values of inverted profiles between experiments were compared in an attempt to optimize the test configuration. This proposed approach was typically much more efficient compared to solely conducting field tests by trial-and-error.

### 1.2.2 Task 2 – Field Experiments on Site with the Presence of Sinkholes

In conjunction with the laboratory synthetic simulation, field investigation of two typical Florida sites with histories of sinkholes (e.g., past activity) were investigated. The work focused on identifying the sensitivity of the 2-D technology in locating sinkholes, chimneys and/or anomalies. Multiple lines of at least 200 ft with phone spacing of 5 to 10 ft were used. Of interest were the sensitivity (i.e., grid size) and separate inversion of shear and compression waves which assisted in not only identifying soils, but also voids and possible presence of water within the voids. Also, since the analysis was 2-D, the location of each line relative to the anomaly and its size were investigated.

### 1.2.3 Task 3 – Analysis of Field Seismic Data and Comparison to Invasive Tests

All of the field collected data were analyzed using full seismic wave field propagation and inversion algorithms. Data processing (filtering and windowing) was applied to the raw measured data before running inversions, and several inversion runs with different medium mesh sizes were investigated. Finally, the characterized results were compared with the known information of the sinkhole, or compared to results of independent invasive tests (SPT, CPT) to assess the capability of the technique.

Three different sites (University of Florida (UF) campus, US-441, and Newberry, Florida) were investigated. All of the invasive testing was completed by the State Materials Office (SMO) of the Florida Department of Transportation (FDOT). The latter was involved in both SPT and CPT testing. The seismic work was carried out by University of Florida (UF) personnel (site testing) and Clarkson University personnel (FWI inversion). The final report includes results of synthetic modeling, field investigations, inversions and recommendations.

# CHAPTER 2
# FULL WAVEFORM INVERSION METHOD

## 2.1 Forward Modeling

Full waveform analysis of seismic surface waves involved a forward model to characterize particle motion, stresses, etc., within a domain due to surface excitation (i.e., sledge-hammer impacts) and an inversion to update the properties (e.g., Shear, G, and Young's, E, moduli) such that measured particle motions (i.e., via geophones) matched the predicted (i.e., forward) model.

For the forward modeling, two-dimensional elastic wave propagation was described by a set of the first-order linear partial differential equations as follows:

Equations governing particle velocity:

$$\begin{cases} \dot{v}_x = \dfrac{1}{\rho}\left(\sigma_{xx,x} + \sigma_{xz,z}\right) + f_x \\ \dot{v}_z = \dfrac{1}{\rho}\left(\sigma_{xz,x} + \sigma_{zz,z}\right) + f_z \end{cases} \tag{1}$$

Equations governing the stress tensor:

$$\begin{cases} \dot{\sigma}_{xx} = \left(\lambda + 2\mu\right)v_{x,x} + \lambda v_{z,z} + g_{xx} \\ \dot{\sigma}_{zz} = \left(\lambda + 2\mu\right)v_{z,z} + \lambda v_{x,x} + g_{zz} \\ \dot{\sigma}_{xz} = \mu\left(v_{x,z} + v_{z,x}\right) + g_{xz} \end{cases} \tag{2}$$

In these equations, ($v_x$, $v_z$) represented the particle velocity vector; ($f_x$, $f_z$) the body force vector; ($\sigma_{xx}$, $\sigma_{zz}$, $\sigma_{xz}$) the stress tensor; ($g_{xx}$, $g_{zz}$, $g_{xz}$) the traction source tensor (surface loading); $\rho$ the mass density; and $\mu$, $\lambda$ Lamé coefficients (function of G and E). The notations (,$x$ and ,$z$) denoted the spatial derivatives with respect to x and z, and the dot ($\cdot$) denoted a time derivative. Typically, the body forces and traction sources were zeroes everywhere in the medium, except at the source locations where the medium was perturbed.

To solve the wave equations (Eqs. 1 and 2), the classic velocity-stress staggered-grid finite difference scheme in the time domain (Virieux, 1984; 1986) was used in combination with absorbing boundary conditions (Clayton and Engquist, 1977). The code was developed in Matlab where all stresses and particle velocities are calculated in matrix form at each time step (explicit) and then advanced in the time domain. The accuracy of the code (Tran and Hiltunen, 2012b) was already illustrated by comparing its wave field solution to that generated by a finite element method solution provided by the commercial software Plaxis2D.

Since the analysis was two-dimensional, i.e., the wave fields were modeled in a plain strain condition, the active source was modeled as a line (not a point source such as a hammer blow). This discrepancy created near-field three-dimensionally (3-D) which was found to limit capability of the technique in detection of deep voids or small voids (Chapter 4). To reduce these effects, the geometrical spreading correction proposed by Schäfer et al. (2012) was implemented (see Chapter 4).

## 2.2 Model Updating by Gauss–Newton Method

Inversion involved minimizing the residual between the estimated responses obtained by forward simulation and the observed seismic data. The residual was defined as:

$$\Delta \mathbf{d}_{i,j} = \mathbf{F}_{i,j}(\mathbf{m}) - \mathbf{d}_{i,j} \tag{3}$$

where $\mathbf{d}_{i,j}$ and $\mathbf{F}_{i,j}$ ($\mathbf{m}$) represented the observed data (e.g., particle motions) and the estimated data associated with the model $\mathbf{m}$ (e.g., E and G), and indices $i$ and $j$ denoted the $i$-th shot and $j$-th receiver, respectively.

To avoid the influence of the source on the estimation during inversion, the residual ($\Delta \mathbf{d}_{i,j}$) was modified using cross-convolved wave fields (Cheong et al., 2006; Choi and

Alkhalifah, 2011). That is, for each shot the estimated wave fields were convolved with a reference trace from the observed wave field, and the observed wave fields were convolved with a reference trace from the estimated wave field as:

$$\Delta \mathbf{d}_{i,j} = \mathbf{F}_{i,j}(\mathbf{m}) * \mathbf{d}_{i,k} - \mathbf{d}_{i,j} * \mathbf{F}_{i,k}(\mathbf{m}) \tag{4}$$

where $\mathbf{d}_{i,k}$ and $\mathbf{F}_{i,k}$ $(\mathbf{m})$ were the reference traces from the observed and estimated data, respectively, at the *k*-th receiver position. The symbol * denoted the convolution.

To minimize the residual, a least-squares error E($\mathbf{m}$) was introduced as:

$$\begin{aligned} &\mathrm{E}(\mathbf{m}) = \frac{1}{2}\Delta \mathbf{d}^t \, \Delta \mathbf{d}, \\ &\textit{and} \\ &\Delta \mathbf{d} = \left\{ \Delta \mathbf{d}_{i,j}, \ i = 1,...NS, \ j = 1...NR \right\} \end{aligned} \tag{5}$$

where the superscript *t* denoted the matrix transpose. *NS* and *NR* were the number of shots and receivers, respectively. The term $\Delta\mathbf{d}$ represented a column vector, which is the combination of residuals $\Delta\mathbf{d}_{i,j}$ for all shots and receivers. If the number of time steps for each shot was *NT*, the size of $\Delta\mathbf{d}$ was $NT \times NS \times NR$. The Gauss–Newton method minimized the error E($\mathbf{m}$) by updating model parameters at the (*n+1*)-th iteration from the *n*-th iteration (Tarantola, 1987) as:

$$\mathbf{m}^{n+1} = \mathbf{m}^n - [\mathbf{J}^t \, \mathbf{J}]^{-1} \mathbf{J}^t \, \Delta \mathbf{d} = \mathbf{m}^n - [\mathbf{H}_\mathbf{a}]^{-1} \mathbf{J}^t \, \Delta \mathbf{d} \tag{6}$$

where $\mathbf{H}_\mathrm{a}$ represented the approximate Hessian matrix and $\mathbf{J}$ the Jacobian matrix, which may be obtained by taking the partial derivatives of seismograms with respect to parameters of model $\mathbf{m}$ and convolving with the reference traces (Tran and McVay, 2012):

$$\mathbf{J}_{i,j} = \frac{\partial \, \mathbf{F}_{i,j}(\mathbf{m})}{\partial \, m_p} * \mathbf{d}_{i,k} - \mathbf{d}_{i,j} * \frac{\partial \, \mathbf{F}_{i,k}(\mathbf{m})}{\partial \, m_p}, \ \ i = 1...NS, \ j = 1...NR, p = 1...M. \tag{7}$$

The subscript *p* represented the model parameter, and *M* the number of model parameters. If the whole matrix **J** were calculated, the resulting size would be $NT \times NS \times NR$ rows and *M* columns. The partial derivative of seismograms $\left( \frac{\partial \mathbf{F}_{i,j}(\mathbf{m})}{\partial m_p} \text{ or } \frac{\partial \mathbf{F}_{i,k}(\mathbf{m})}{\partial m_p} \right)$, with respect to each model parameter, were directly computed from the residual of two seismograms with and without perturbation of the model parameter. Perturbing individual model parameters required ($M$ +1) forward modeling simulations for one shot or a total of $NS \times (M + 1)$ simulations for the calculation of the matrix **J**. Thus, significant computer time was required for cases of a few thousand unknowns presented herein. To reduce the computer time, this work followed an efficient technique (Sheen et al., 2006) using virtual sources and reciprocity of wave fields, which required only (*NS*+*NR*) simulations for the calculation of the matrix **J.** In addition, updating model parameters with Eq. 6 did not require storing the whole matrix **J**. For details, see the work of Sheen et al. (2006).

Using the Gauss–Newton method for a full waveform inversion, regularization was important to maintaining a stable optimization. This study followed the approach presented by Sheen et al. (2006) as:

$$\mathbf{m}^{n+1} = \mathbf{m}^n - \alpha^n [\mathbf{J}^t \mathbf{J} + \lambda_1 \mathbf{P}^t \mathbf{P} + \lambda_2 \mathbf{I}^t \mathbf{I}]^{-1} \mathbf{J}^t \Delta\mathbf{d} \quad (8)$$

Their suggested coefficients of $\lambda_1$ = 0.05 and $\lambda_2$ =0.0005 were used in this work. **I** was the identity matrix, and **P** the matrix whose elements were determined using a 2-D Laplacian operator:

$$P_p \Delta\mathbf{m} = (\Delta m_p)^E + (\Delta m_p)^W + (\Delta m_p)^N + (\Delta m_p)^S - 4(\Delta m_p) \quad (9)$$

where the superscripts *E*, *W*, *N*, and *S* refer to four adjacent cells (left, right, above, and below) of the cell referring to the model parameter $m_p$, and $P_p$ was the *p*-th row of the matrix **P** whose elements were either 1, –4, or 0. Lastly, the optimal step length ($\alpha^n$) in the Eq. 8 was determined (Pica et al., 1990) as:

$$\alpha^n \cong \frac{[\mathbf{J}^t g^n]^t [\mathbf{F}(\mathbf{m}^n) - \mathbf{d}]}{[\mathbf{J}^t g^n]^t [\mathbf{J}^t g^n]},$$
$$g^n = [\mathbf{J}^t \mathbf{J} + \lambda_1 \mathbf{P}^t \mathbf{P} + \lambda_2 \mathbf{I}^t \mathbf{I}\ ]^{-1} \mathbf{J}^t [\mathbf{F}(\mathbf{m}^n) - \mathbf{d}]. \quad (10)$$

From study on the synthetic models (Chapter 3), the optimal step lengths were found to typically vary from 0.5 to 0.9. For simplicity, a constant value of 0.5 was used through all the iterations for cases presented herein to reduce the required computer RAM for storing the whole matrix **J**.

# CHAPTER 3
# SYNTHETIC MODELING

## 3.1 Introduction

Synthetic models refer to earth models whose velocity profile (i.e., cell information: E and G) was assumed or known a priori. Specifically, using a known velocity profile, surface wave field data (e.g., particle velocities) was calculated (i.e., forward modeling) for an assumed test layout (set of sources and receivers). This surface wave field data were then input to the inversion program as if the data were collected from a field test, and velocity structure was back-computed (i.e., inversion) from the surface wave field data with a simple initial velocity profile (e.g., linear increasing with depth). Theoretically, the back-computed velocity profile should be the same as the model used to generate surface wave field data.

Synthetic model studies were generally performed for two reasons. The first objective was to assess the ability of the inversion technique to identify and delineate subsurface features that were of interest on a test site. For instance, if synthetic surface wave data were generated (forward modeling) with certain features (e.g., voids, low-velocity zones, horizontal variability), and the inversion was unable to delineate these features, then there would be no point in conducting an actual field test and subsequent inversion. Secondly, in conducting model studies in which the "answer" was known, an analysis protocol (e.g., constraints on variables or interdependence) could be developed to systematically and consistently analyze wave field data to derive improved velocity profiles. For instance, the use of low frequency inversion as velocity profile input to higher frequency inversions was an outcome of this study.

### 3.2 Modeling an Embedded Air-Filled Void

The synthetic model for this study consisted of three layers with an embedded air-filled void (blue zone in the third layer) (see Fig. 3-1a). It mimicked a real soil profile made at Newberry, Florida, which consisted of two upper soil layers underlain by limestone. The upper, approximately 5-m (16 ft) layer, was medium dense fine sand, overlying 5 m (16 ft) of silty sand. The shear wave (S-wave) velocities of the materials were set at 200 m/s (656 ft/s) for the first soil layer, 400 m/s (1312 ft/s) for the second soil layer, 700 m/s (2297 ft/s) for the limestone, and zero for void. The pressure wave (P-wave) velocity was generated from the S-wave velocity assuming a constant Poisson's ratio of 0.3 for the whole domain.

A finite-difference code (Tran and Hiltunen, 2012b) was used for the forward modeling to generate the surface synthetic waveform data set (i.e., geophone velocity data). The synthetic waveform data was recorded from 24 receivers spaced every 1.5 m (5 ft) from station 0.75 m (2.5 ft) to 35.25 m (105 ft), due to 25 shots (20-lb sledgehammer) at 1.5 m (5 ft) spacing starting from 0 m to 36 m on the ground surface. For start of the inversion, the initial profile for the domain consisted of having S-wave velocity increasing with depth [100 m/s (328 ft/s) at the surface to 600 m/s (1968 ft/s) at the bottom] and P-wave velocity was generated from the S-wave velocity with a constant Poisson's ratio of 0.3 for the whole domain as shown in Fig. 3-1b. Note, in the initial model, no consideration of any void or any heterogeneity, except for layering, was characterized. Four inversion runs were performed on the data sets at four central frequency ranges, i.e., 5, 10, 15, and 20 Hz. The first run began with the lowest frequency range (central frequency of 5 Hz) using the initial model in Fig. 3-1b. Subsequent runs for the other central frequencies, i.e., 10, 15, and 20 Hz were completed using the inverted result of each of the lower frequencies as initial models for the subsequent higher frequency analysis. During inversion,

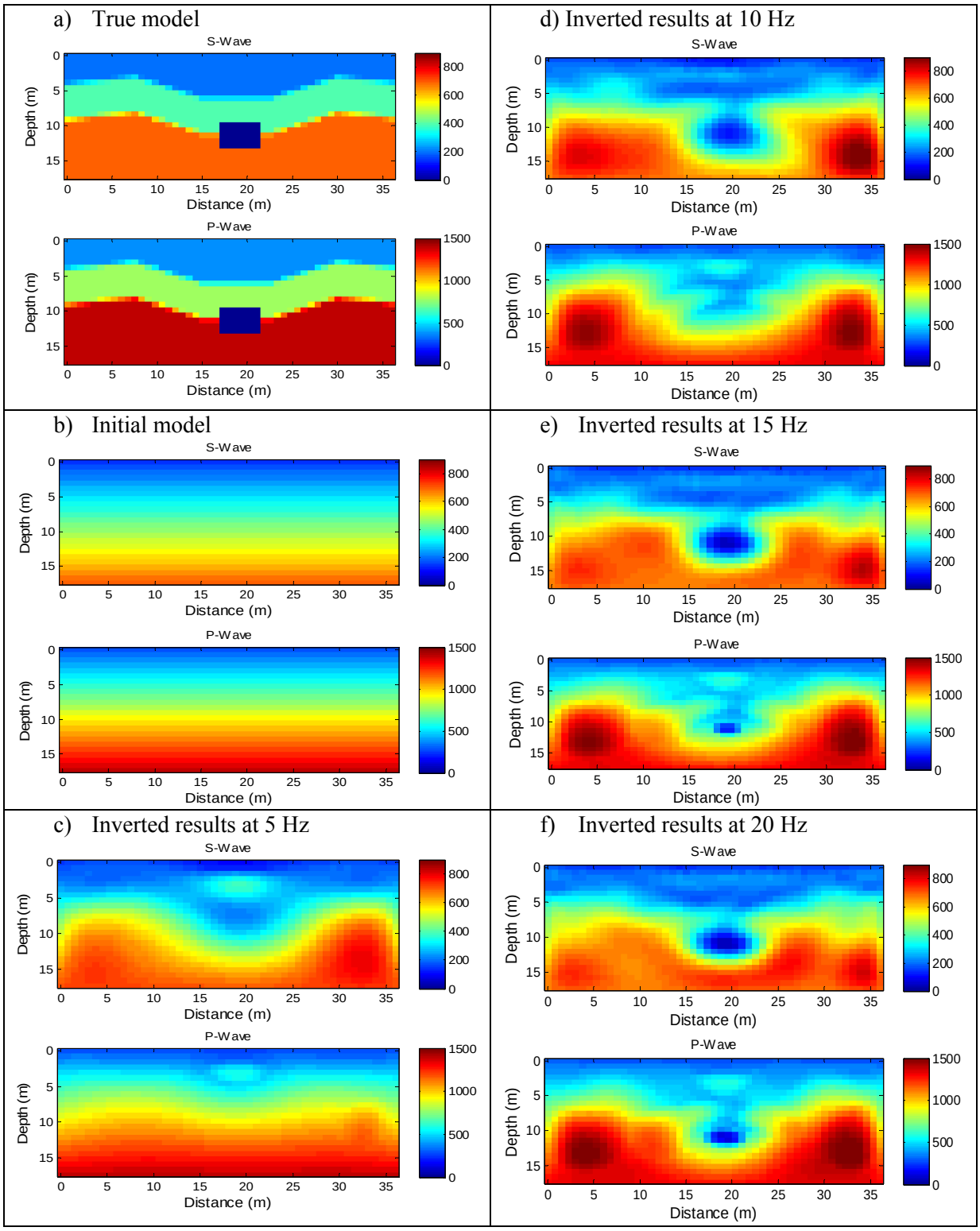


**Figure 3-1.** Synthetic model of S-wave and P-wave velocities (m/s): a) True model (Vs = Vp = 0 for void); b) Initial model; c) Inverted model at 5 Hz; d) Inverted model at 10 Hz; e) Inverted model at 15 Hz; and f) Inverted model at 20 Hz.

S-wave and P-wave velocities of cells were updated independently, and each run was stopped after 20 iterations when the estimated and measured waveform data were similar to one another. The complete analysis (i.e., four frequency inversions) required approximately three hours on a laptop computer (4 cores with 2 GHz each and 8 GB of memory).

The comparison between the estimated and observed surface data for one shot for the last inversion run (20 Hz central frequency) is presented in Fig. 3-2. Evident is that observed and estimated waveforms are quite similar and the residuals (i.e., differences) were very small. The inverted results for all four inversions (frequency ranges of 5, 10, 15, and 20 Hz) are shown in Figs. 3-1c, d, e, and f, respectively. From a comparison of the true model (Fig. 3-1a) against the final inverted model (Fig. 3-1f), the following is suggested: 1) soil layering was accurately characterized (e.g., surface undulations); 2) the presence, location, and shape of the void was successfully identified, i.e., S-wave close to 0; and 3), the P-wave velocity profile (solved independently of S-wave velocity) was also recovered.

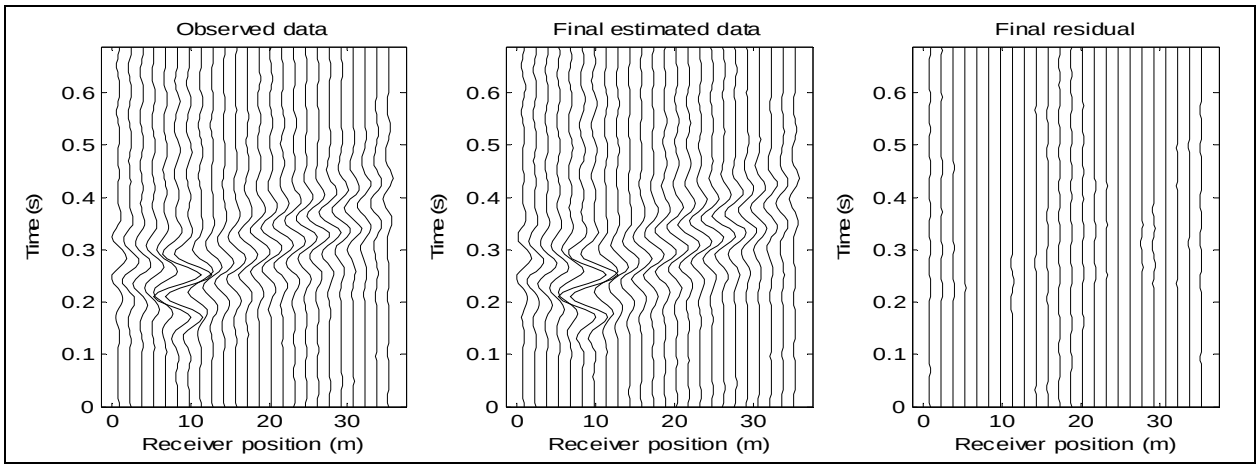


**Figure 3-2.** Comparison of the observed and estimated data set of one shot for inversion run at the frequency range of 20 Hz.

### 3.3 Modeling a Water-Filled Embedded Void

Of great interest was identifying water-filled voids in soil and rock masses. For instance, the P-wave velocities in water and limestone are similar, but their S-wave velocities are quite different (zero in void). Similar to the air-filled model, a water-filled synthetic model (see Fig. 3-3a) consisting of 3 layers with an embedded water-filled void (blue zone in the third layer) was developed. The S-wave velocities of materials were 200 m/s (656 ft/s) and 400 m/s (1312 ft/s) for the upper soil layers, 700 m/s (2296 ft/s) for limestone, and zero for the void. The groundwater table was set at a depth of 8 m (26 ft). The P-wave velocities above the water table were generated from the S-wave velocity data with an assumed Poisson's ratio of 0.3. The P-wave velocity below the water table was selected as 1500 m/s (4921 ft/s), which was the same as the P-wave velocity in water.

Surface data was recovered from 24 receivers spaced 1.5-m (5-ft) apart [station 0.75 m (2.5 ft) to 35.25 m (115.5 ft)], employing 25 surface shots (20lb sledgehammer) at 1.5-m (5-ft) spacing starting from 0 m to 36 m (0 to 120 ft). For the start of the inversion, the initial S-wave velocity profile of the soil/rock mass was set at 100 m/s (328 ft/s) at the surface and linearly increased with depth to 600 m/s (1968 ft/s) at the bottom; the P-wave velocity was computed from the S-wave velocity, assuming a constant Poisson's ratio of 0.3 for the whole domain as shown in Fig. 3-3b. Note, no prior information concerning the void or the water table was assumed in the initial model.

Similar to inversion of the air-filled model, four inversion runs were performed on the synthetic data sets using four different frequency ranges with central frequencies of 5, 10, 15, and 20 Hz. Each analysis (e.g., 5 Hz) required approximately 4 hours on a laptop computer (4 cores with 2 GHz each and 8 GB of memory). The first run began with the lowest frequency

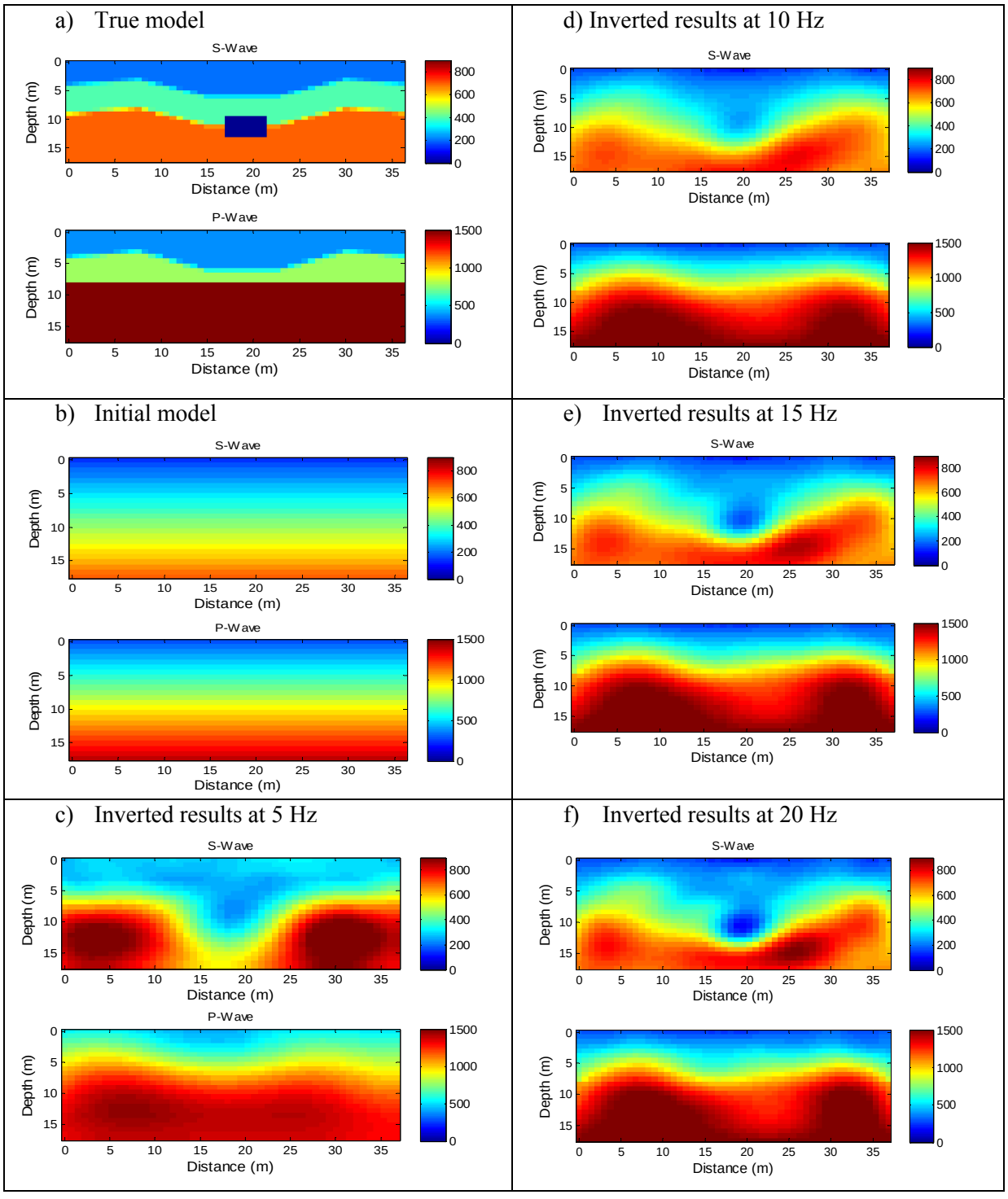


**Figure 3-3.** Synthetic model of S-wave and P-wave velocities (m/s): a) True model (Vs = 0, Vp = 1500 for void filled by water); b) Initial model; c) Inverted model at 5 Hz; d) Inverted model at 10 Hz; e) Inverted model at 15 Hz; and f) Inverted model at 20 Hz.

range (central frequency of 5 Hz) and the assumed initial model, Fig. 3-3b. Subsequent runs for central frequencies of 10, 15, and 20 Hz were completed with the inverted result of each lower frequency used as the initial model for the next higher frequency run. During each inversion, both S-wave and P-wave velocities of all cells were updated independently, and each run was stopped after 20 iterations. The inverted results of the 4 runs are shown in Figs. 3-3c, d, e, and f for analysis of the data at 5, 10, 15, and 20 Hz, respectively. From a comparison of the true model (Fig. 3-3a) with the final inverted model (Fig. 3-3f), it was evident that the soil layers were accurately characterized, as well as the presence, location, and shape of the void successfully identified in S-wave profile. P-wave profile was also generally recovered, especially inverted P-wave velocities below the water table [8-m (26-ft) depth] which were close to the true value 1500 m/s (4921 ft/s).

### 3.4 Summary of Synthetic Modeling

A number of important findings were obtained with the synthetic modeling: 1) presence of voids (air- or water-filled) were detectable with seismic full waveform inversions; 2) independent assessment of S and P velocity profiles in complex domains (i.e., layering, voids, etc.) were possible; and 3) simple linear velocity profiles (S- and P-waves) could be used as initial conditions in the full waveform analysis, if low frequencies (e.g., 5 Hz) were used to start the inversion. The first two findings were significant because not only voids are detectable, but other forms of heterogeneity were discernible, e.g., different types of soil (cohesionless and cohesive, i.e., Poisson's ratio), water-filled void, etc. The finding in item 3 is important because it shows the inversion process was robust, i.e., converged on a solution with simple initial conditions, not requiring complex initial analysis (e.g., simulated annealing). The next step recovered real field data for analysis/inversion, which involved noise, 3-D effects, etc.

# CHAPTER 4
# FIELD EXPERIMENTS

Based on the success of FWI in detecting heterogeneity and anomalies, i.e., air-filled and water-filled embedded voids in the synthetic models, full-scale field testing of a number of Florida sites was undertaken. For the field applications, FWI was performed on problems of an increasing level of complexity. The first problem analyzed was an embedded culvert with known size and depth; the second was a deposit with a known low-velocity anomaly; the third had open chimneys (i.e., sinkholes); and the final was a natural occurring site with no identifiable sinkhole, but where multiple line analyses located a buried sinkhole later verified with invasive testing. The results are presented in that order with discussion of input, output and associated verification (e.g., invasive testing).

## 4.1 UF Campus Test Site with an Embedded Culvert

The FWI algorithm was first tested on a basic profile with a known anomaly, i.e., a buried culvert (storm drain) located on the University of Florida campus. From observed manholes at both ends, the culvert was 1.2 m (4 ft) in diameter, filled with air, and embedded 3.5 m (11 ft) below the ground surface as shown in Fig. 4-1.

Seismic tests were conducted perpendicular to the direction of the culvert using a linear array of twenty-three 4.5-Hz geophones at a spacing of 0.6 m (2 ft), for a total receiver spread of 13.4 m (44 ft) [station 0.3 m to 13.7 m (1 ft to 45 ft)]. Seismic energy was created by vertically striking a 15-cm (6 inch) square metal plate with a 45 N (10 lb) sledgehammer. Twenty-four shots at 0.6-m (2 ft) spacing were recorded, for a total shot spread of 14.0 m (46 ft) [station 0.0 m to 14.0 m (0 to 46 ft)]. Due to the limited test space (trees), the culvert was only 4 m (13 ft) from the beginning of the source/receiver array, instead of the middle as shown in Fig. 4-1.

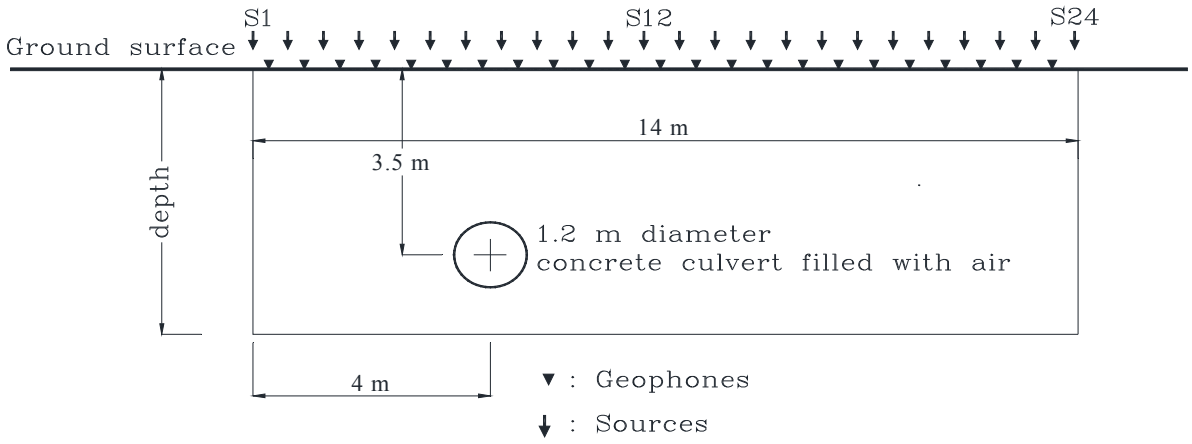


**Figure 4-1.** UF campus site: Culvert location and seismic testing configurations.

Since the FWI analysis was 2-D, i.e., the wave fields had to be modeled in a plain strain condition, the active source being modeled as a line (not a point source, i.e., hammer blow). This discrepancy created near-field 3-D effects that might have limited capability of the technique in detection of deep voids or small voids near the surface. To reduce the 3-D effects, the geometrical spreading correction proposed by Schäfer et al. (2012) was implemented in the FWI algorithm. The geometrical corrections transformed the point-source wave into an equivalent line-source wave field by using amplitude and phase transformations. The amplitude transformation was mandatory due to the misfit definition with the L2 norm. The amplitude-decay of waves excited by a point (measured) and a line source (modeled) varied differently, especially near the source. The modeled wave field was therefore adjusted by an offset dependent correction factor of the form $y(r) = A \cdot r^{\alpha}$, where $r$ was the distance from the source to the geophone. The A coefficient and the exponent $\alpha$ was fitted by an iterative least squares inversion which minimized the energy of the waveform residuals. The values of $A$ and $\alpha$ were estimated at the beginning of the inversion and kept constant for all iterations. The phase transformation was simply the convolution of the point-source wave field with the inverse square root of time ($t^{-1/2}$).

To avoid the inversion being trapped in local minima, an appropriate initial model (S- and P-wave velocity profiles) was required. The initial model could have been generated by using global inversion techniques, such as genetic algorithm (Tran and Hiltunen, 2012a) or the simulated annealing approach (Tran and Hiltunen, 2012b; Cercato, 2011). Even though these methods likely produced a global solution, they required significant computer time. Alternatively, from the synthetic model study, it was found that a simple increasing velocity profile with depth was sufficient to start the 2-D inverse analysis, if sufficient low frequency (e.g., 5 Hz) was used to start the analysis. For simplicity, an estimate of the initial velocity profile was obtained via a spectral analysis of the measured data. Figure 4-2a presents a normalized power spectrum obtained using the cylindrical beamformer technique (Tran and Hiltunen, 2008) for the measured data from the shot at station 0 m. As evident in Fig. 4-2b, the energy of the measured wave field concentrated in a narrow band with the Rayleigh wave velocities observed to vary from 200 to 300 m/s (656-984 ft/s). Therefore, the S-wave velocity, which was slightly larger than Rayleigh wave velocity profile, was selected to range from 200 to 350 m/s (656-1148 ft/s).

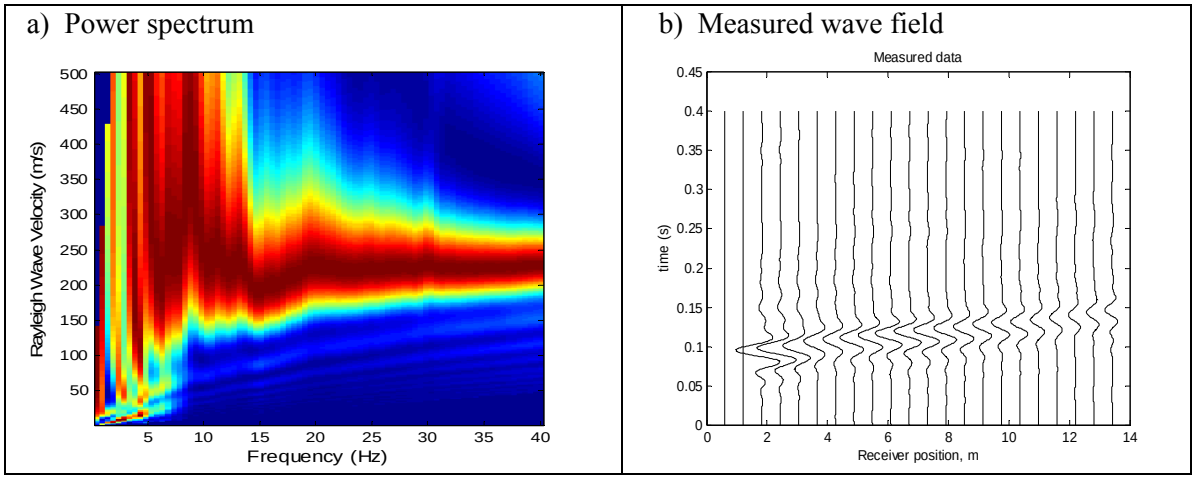


**Figure 4-2.** UF campus site: a) Power spectrum for one shot at the end of geophone array; and b) Measured wave field.

The mass density throughout the model was kept constant at 1800 kg/m$^3$ (112 lb/ft$^3$) for all inversions. Efforts to invert the mass density of the medium from the measured wave fields were shown to be unsuccessful. The latter may be explained by the insensitivity of energy in surface Rayleigh waves (Richart et al., 1970) to mass density (Nazarian, 1984).

Similar to the synthetic model, four inversion runs were performed with central frequencies varying from 10, 15, 20, and 25 Hz, beginning from the lowest frequency. Again, the initial model for higher frequency analysis was the solution of the prior lower central frequency analysis. The medium, 14 m × 6 m (46 ft × 20 ft), was divided into 920 cells with dimensions of 0.3 m × 0.3 m (1 foot × 1 foot) . The final inversion results at 25 Hz are shown in Fig. 4-3. It was observed that the presence, location, as well as S-wave and P-wave velocity values (close to 0) of the void (open culvert), were successfully identified in both S-wave and P-wave velocity profiles.

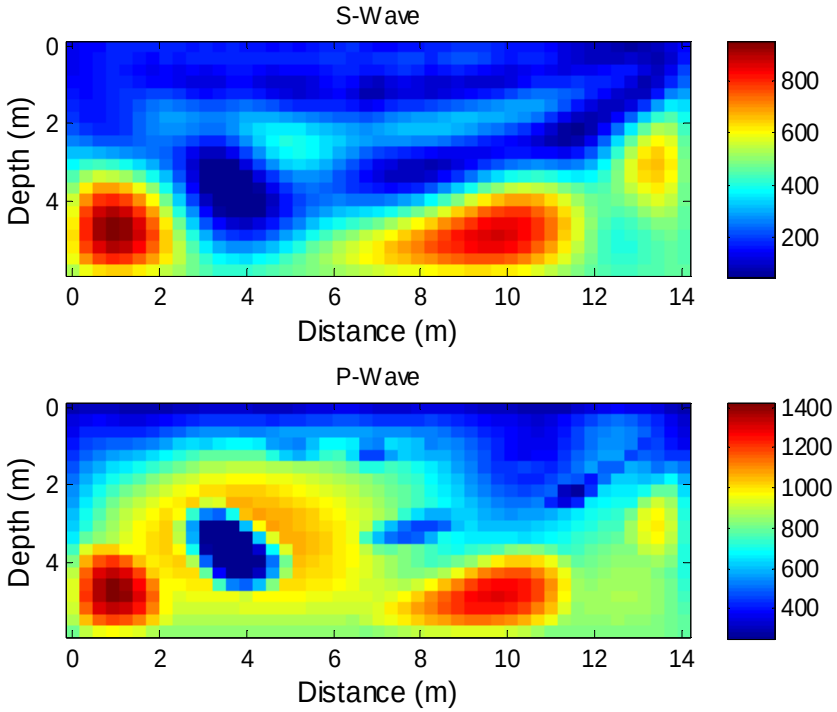


**Figure 4-3.** UF campus site in situ test results: S-wave velocities and P-wave velocities (m/s).

### 4.2 US-441 Test Site with an Embedded Low-Velocity Anomaly

This test site was located on the shoulder of US-441 Highway, in Marion County, Florida. FDOT District 5 asked the researchers if they were interested in analyzing an emergency repair on US-441 due to a sinkhole opening following Tropical Storm Debby. The seismic test was conducted using a linear array of twenty-four 4.5-Hz geophones at a spacing of 1.5 m (5 ft), for a total receiver spread of 34.5 m (115 ft) [station 0.75 m to 35.25 m (2.5 ft to 117.5 ft)]. The seismic energy was created by vertically striking a 150-mm (6-inch) square metal plate with a 20 lb sledgehammer. Twenty-five shots at 1.5-m (5-ft) spacing were recorded, for a total shot spread of 36.0 m (120 ft) [station 0.0 m to 36.0 m (0 to 120 ft)]. Cone penetration tests (CPT) were also conducted by District 5 personnel to verify the inverted S-wave and P-wave profiles (velocities) with depth.

To run the inversion, a representative set of initial properties for the 2-D model was important. From the study of synthetic data, a linear increasing velocity profile without horizontal variability was sufficient. For simplicity, an estimate of the initial model was again established via a spectral analysis of the measured data. Figure 4-4a presents a normalized power spectrum obtained using the cylindrical beamformer technique from the measured shot data at station 0 m (Fig. 4-4b). The observed energy in the measured wave field was concentrated in a narrow band with the Rayleigh wave velocities in the range of 200 to 350 m/s (656 to 1148 ft/s). The S-wave velocity, which was slightly larger than Rayleigh wave velocity, was therefore taken in the range of 200 to 400 m/s (656 to 1312 ft/s). Also, the depth of the medium analyzed was assumed to be one-half the length of the total geophone layout (ensuring that signals would pass through domain of interest). Consequently, with a range of S-wave velocities, depth of the model, and initial 1-D assumption (i.e., no initial variation in horizontal direction), a linear

increasing S-wave velocity from 200 m/s (656 ft/s) at the surface to 400 m/s (1312 ft/s) to a depth of 18 m (60 ft) over a length of 36 m (120 ft) was selected as the initial profile. The initial P-wave velocity for the domain was calculated from the S-wave velocities assuming that the initial Poisson's ratio throughout the domain was 0.25.

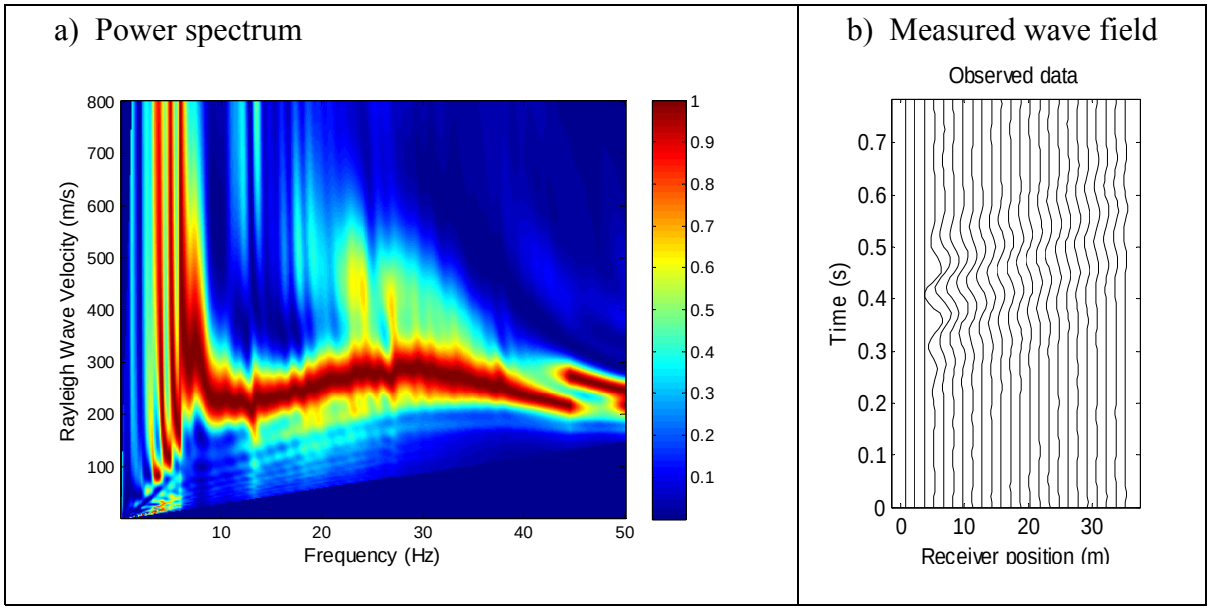


**Figure 4-4.** US-441 site: a) Normalized power spectrum of the real data from one shot at station 0 m; and b) Measured wave field.

Three separate inversion runs were performed on the filtered data sets using three central observed frequency ranges: 6, 10, and 15 Hz. Ricker wavelets having central frequencies of 6, 10, and 15 Hz were used to model the active source (sledgehammer) for the forward modeling of each analysis. For the finite difference solution, a grid size of 0.75 m (2.5 ft) was selected, i.e., equal to half the spacing of each receiver. Note, the criterion of 10 mesh points per wavelength (Virieux, 1986) also suggested a grid size of 0.75 m (2.5 ft) to accurately model a wave field up to a maximum frequency of 26 Hz (velocity/max frequency/10 = 200/26/10 ≈ 0.75 m = 2.5 ft)

and was subsequently used for all three inversion runs. Each inversion run required approximately one hour on a laptop computer (4 cores with 2 GHz each and 8 GB of memory).

The first run began with the lowest frequency range (central frequency of 6 Hz) using the assumed initial model shown in Fig. 4-5a. Subsequent runs for central frequencies of 10 and 15 Hz were completed using the inverted result of each lower frequency as the initial model for the next higher frequency's run. During inversion, both S-wave and P-wave velocities of all cells were updated independently, and each run was stopped after 20 iterations.

The observed surface waveforms, the estimated surface waveforms, and residuals (difference between observed and estimated) associated with the final inverted model are shown horizontally in Fig. 4-5a through c for the shots at stations 0, 12, and 24 m (0, 40, and 80 ft), respectively. As evident, the observed and estimated data were very similar across the entire range of offsets, and the residuals were small except at receivers near the sources which could be attributed to the near field effects (i.e., non-plane strain).

The initial model is shown in Fig. 4-6a with inverted results of the three runs shown in Figs. 4-6b, c and d for analysis of the data at 6, 10, and 15 Hz, respectively. The final inverted S-wave profile (Fig. 4-6d, top) shows a reverse profile with a low-velocity zone embedded at 9- to 14-m depth (30-47 ft), along with high lateral and vertical variations in limestone boundaries [S > 800 m/s (2624 ft/s)] at the bottom of profile. Also, it should be noted that the full waveform inversion did not require any prior information on the weaker zone, i.e., only the linearly increasing initial model (Fig. 4-6a). Finally, the inverted P-wave profile (Fig. 4-6d, bottom) was consistent with the estimated S-wave profile.

The Poisson's ratio profile was also subsequently calculated from the independently determined S-wave and P-wave velocities (Fig. 4-6d) and shown in Fig. 4-7. The computed

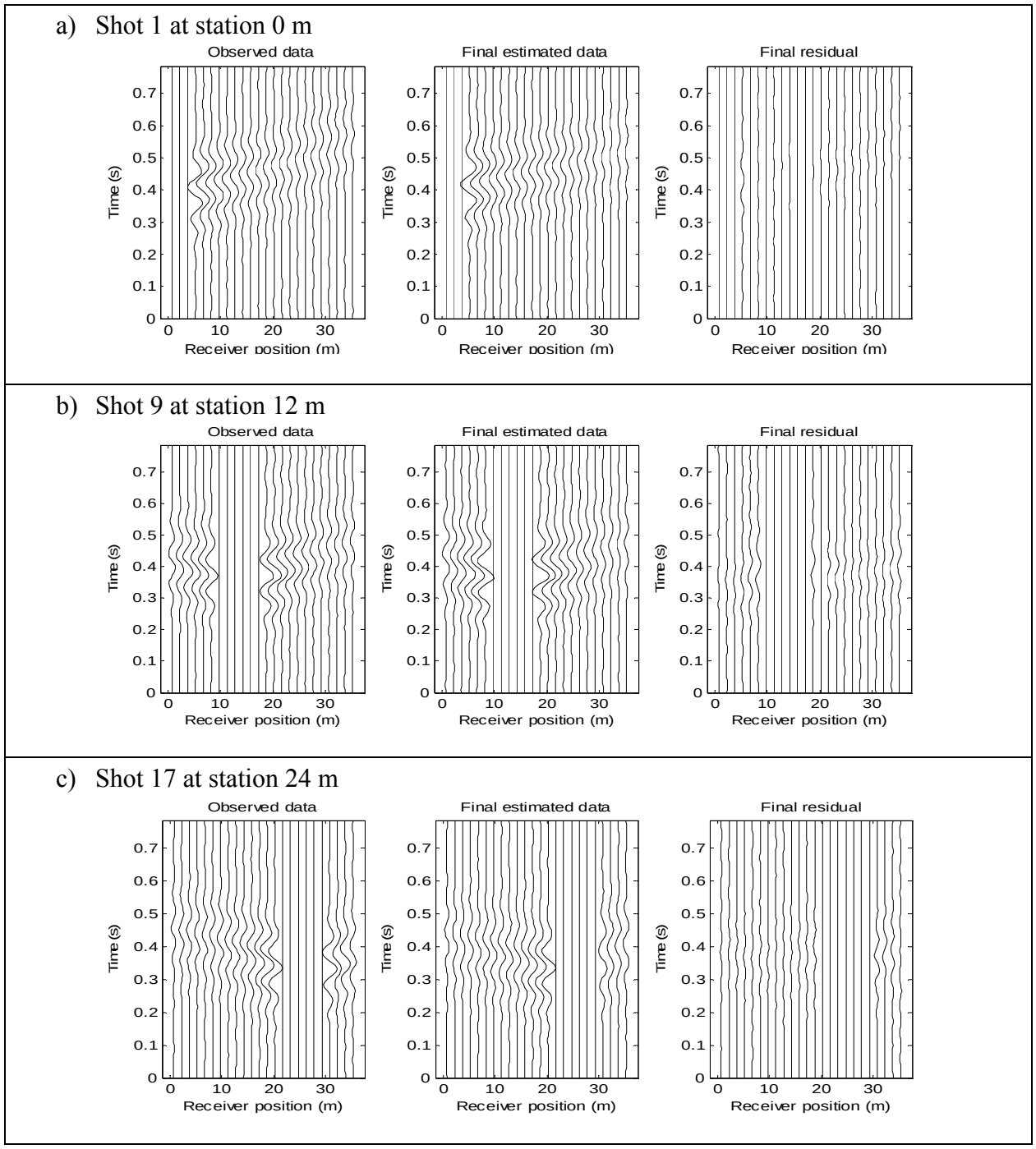


**Figure 4-5.** US-441 site: Comparison between observed and estimated data for shots at: a) 0 m, b) 12 m, and c) 24 m.

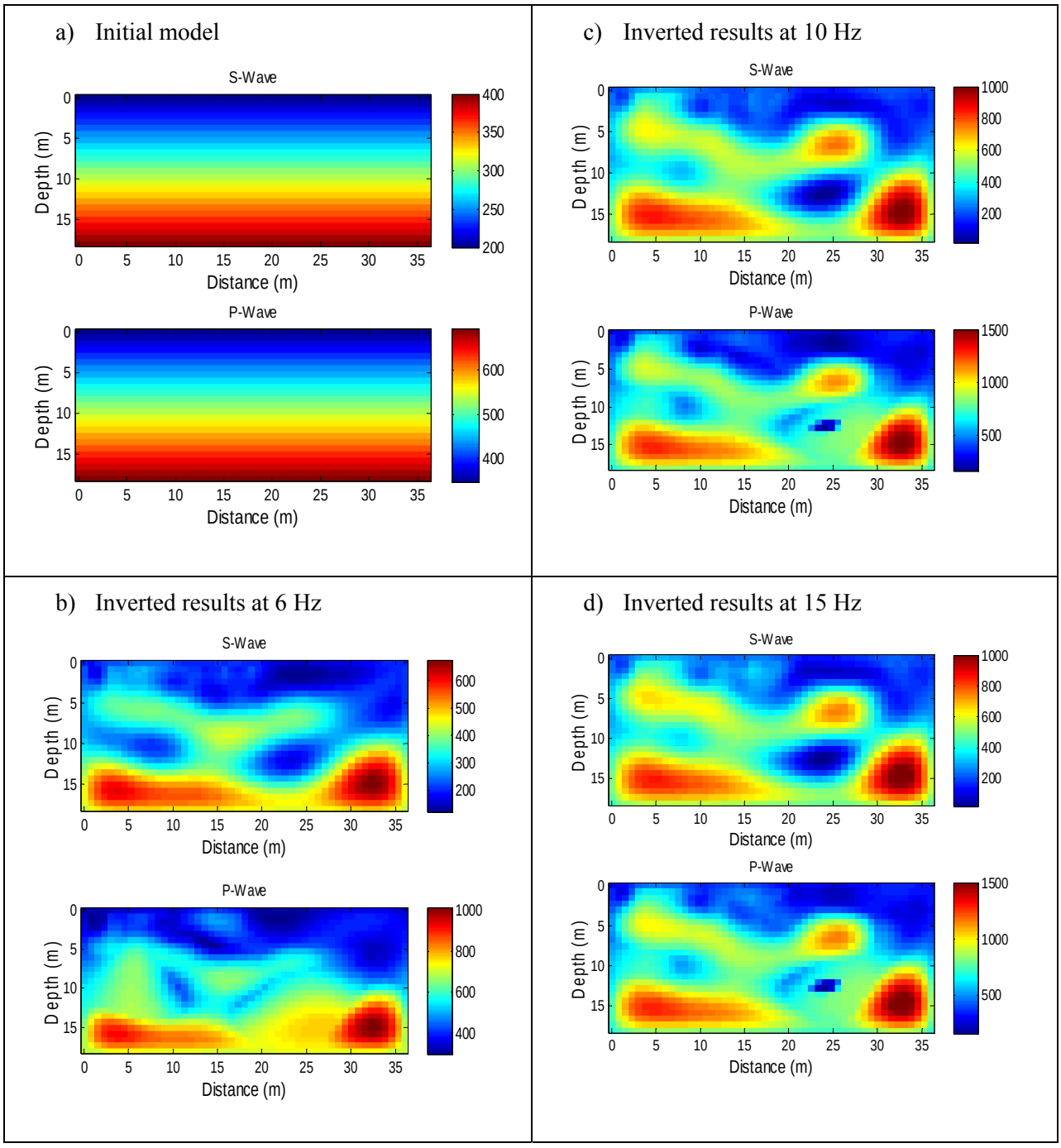


**Figure 4-6.** US-441 site FWI results of S-wave and P-wave velocities (m/s): a) Initial model; b) Inverted model at 6 Hz; c) Inverted model at 10 Hz; and d) Inverted model at 15 Hz.

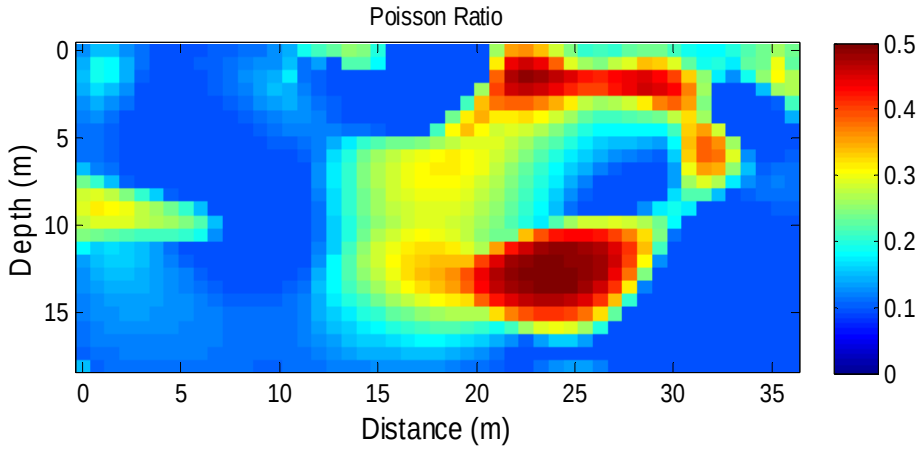


**Figure 4-7.** US-441 site: Poisson's ratio.

Poisson's ratio seemed consistent to S-wave profiles. High values (0.35 to 0.50) were found for low velocity zones (blue area in Fig. 4-6d) that were possibly clay or silt. Low values (0.1 to 0.2) were found for high velocity zones (red and yellow areas in Fig. 4-6d), which were sand and limestone.

Of interest was the comparison of CPT tip resistance, $q_c$, (soil strength) versus wave speed ($q_c$ was generally correlated to Vs). Shown in Fig. 4-8 are the CPT tip resistance ($q_c$) and S-wave velocity (Vs) versus depth for a sounding located 21 m (70 ft) from the origin. It appeared higher strengths, i.e., stiff (high-velocity) zone occurred from 4 to 9 m (13 to 30 ft), a soft (low-velocity) or lower strength zone occurred from 9- to 14-m depth (30 to 47 ft), and the top of bedrock occurred at about 14-m depth (47 ft). For a better correlation between Vs and $q_c$, higher frequencies (30-40 Hz generated by a smaller sledgehammer) might be needed to achieve higher resolution (smaller cells) of Vs at shallow depths. Note, using the horizontal wave speeds from cell to cell, the horizontal spatial correlation structure needed for foundation design (e.g., Klammler et al., 2010) could be readily assessed.

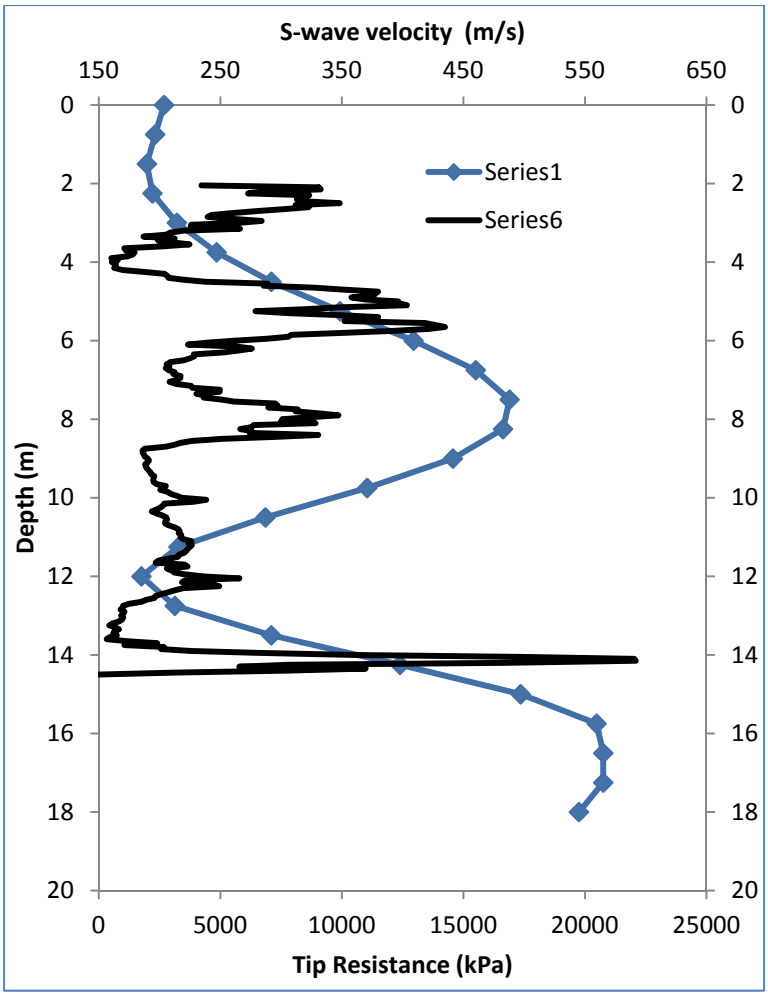


**Figure 4-8.** US-441 site: CPT tip resistance and S-wave velocity at distance 21 m.

### 4.3 South Newberry Test Site with Open Chimneys

The third field test site was an FDOT retention pond located in Newberry, Florida. From invasive tests, the site consisted of medium dense, fine sand and silt 2- to 5-m thick (7 to 16 ft) , overlying a highly variable limestone deposit; the top of limestone varied from 2 m to 10 m (7 to 33 ft) in depth (Tran and Hiltunen, 2011). The site was divided into 26 parallel north–south survey lines equally spaced 3.0 m apart. The lines were labeled A through Z from west to east across the site, and each line was 85.3 m (280 ft) long, with station 0 m located at the southern end of each line.

In addition, FWI was applied to data sets collected in the southern portion of the Newberry site next to open chimneys/sinkholes to investigate the 3-D effects in the 2-D analysis used for the currently coded FWI approach. Two test lines were conducted next to open chimneys as shown in Fig. 4-9. Line 1 was at the grid line G20–G140, next to open Chimneys 1 and 2. Line 2 was at the grid line 95A–95K, perpendicular to Line 1, and next to open Chimneys 2 and 3. Due to safety concerns, the two test lines were conducted 3–4 ft away from the chimneys. FWI near the open chimneys will be discussed prior to description of the 26 parallel north–south lines, which involved searching for a void below the ground surface without any visible surface depressions

### 4.3.1 Line 1 – G20–G140

Line 1 was conducted using a linear array of twenty-four 4.5-Hz vertical geophones at a spacing of 1.5 m (5 ft), for a total receiver spread of 34.5 m (115 ft) [station 0.75 m to 35.25 m (2.5 ft to 117.5 ft)]. The seismic energy was created by striking a 150-mm square metal plate with a 90 N sledgehammer. Twenty-five shots at 1.5 m (5 ft) spacing were recorded, for a total shot spread of 36.0 m (120 ft) [station 0.0 m to 36.0 m (0 to 120 ft)].

For the analysis of the acquired data, a proper initial model of subsurface wave velocity structures (P-wave and S-wave) was required to avoid the inversion being trapped in local minima. The S-wave velocity was determined from spectral analysis of dispersion data with a range from 200 to 400 m/s (656 to 1312 ft/s). A linear increasing S-wave velocity from 200 m/s (656 ft/s) at the surface to 400 m/s (1312 ft/s) to a depth of 18 m (60 ft) (half of test length) over a length of 36 m (120 ft) was considered (see Fig. 4-10a). The initial P-wave velocity for the domain was calculated from the S-wave velocities assuming that the initial Poisson's ratio throughout the domain was 0.25.

a) Test locations

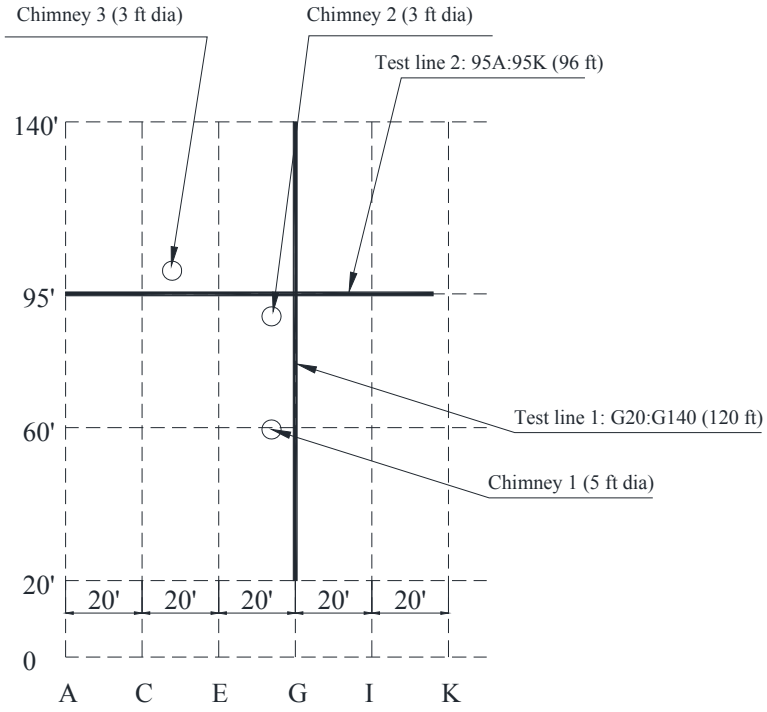


b) Chimney 1

**Figure 4-9.** South Newberry site: a) Test location diagram; b) Chimney 1 photo; c) Chimney 2 photo; and d) Chimney 3 photo (continued on next page).

c) Chimney 2

d) Chimney 3

**Figure 4-9**—continued

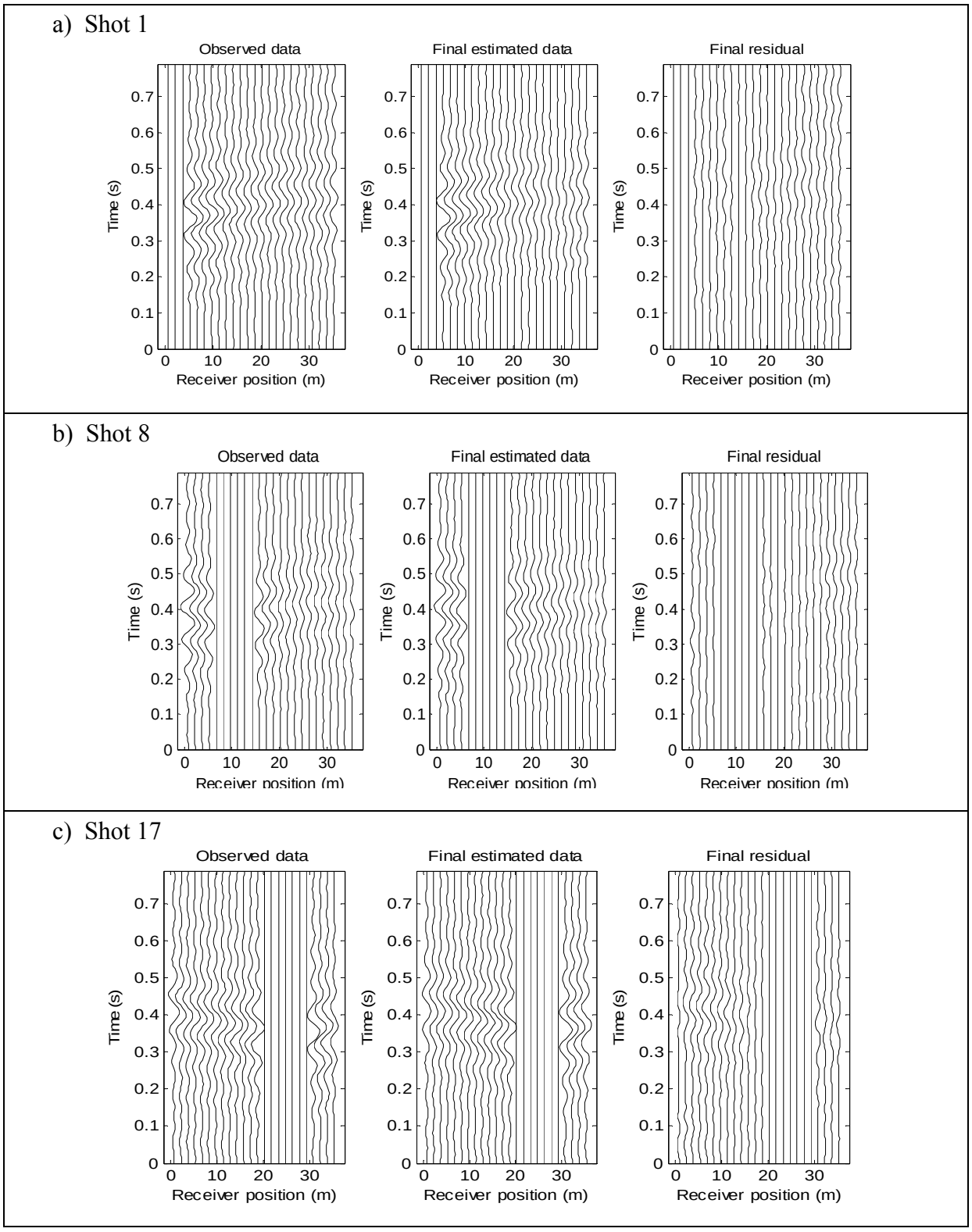


**Figure 4-10.** South Newberry site, Line 1 – G20–G140: Comparison between observed and estimated data for a) Shot 1; b) Shot 8; and c) Shot 17.

Three inversion runs were performed for frequency ranges with central frequencies of 10, 15, and 20 Hz, beginning from the lowest frequency range. The medium of 18 m × 36 m (60 ft × 120 ft) was divided into about 1200 cells of 0.75 m × 0.75 m (2.5 ft × 2.5 ft). During the inversion, S-wave and P-wave velocities of cells were updated independently, and each run was stopped when the observed waveform data and the estimated waveform data were similar. The observed surface waveforms, the estimated surface waveforms, and residuals (difference between observed and estimated) associated with the final inverted model are shown horizontally in Fig. 4-10 for the shots 1, 8 and 17. As evident, the observed and estimated data were very similar across the entire range of offsets, and the residuals were small except at receivers near the sources which could be attributed to the near field effects (i.e., non-plane strain).

The inverted results of the three runs are shown in Figs. 4-11b, c and d for analysis of the data at 10, 15 and 20 Hz, respectively. The final inverted S-wave profile (Fig. 4-10d, top) shows two low-velocity zones at distances 12 m and 22 m (40 and 73 ft), along with high lateral and vertical variations in limestone boundaries [S > 800 m/s (2624 ft/s)] at the bottom of profile. Evidently these anomaly locations were the same as those of the chimneys [i.e., 12 and 22 m (40 and 73 ft)]. The inverted P-wave profile (Fig. 4-10d, bottom) was consistent with the estimated S-wave profile. Chimney 1 of about 1.5-m (5-ft) diameter was also characterized in both S-wave and P-wave images. Chimney 2 of about 0.9-m (3-ft) diameter was not shown, due to 3-D effects. To characterize the smaller chimney, the test line may have needed to be closer to the chimney (typically less than 1 diameter of the chimney), and data at higher frequencies (20–40 Hz) may also have been required.

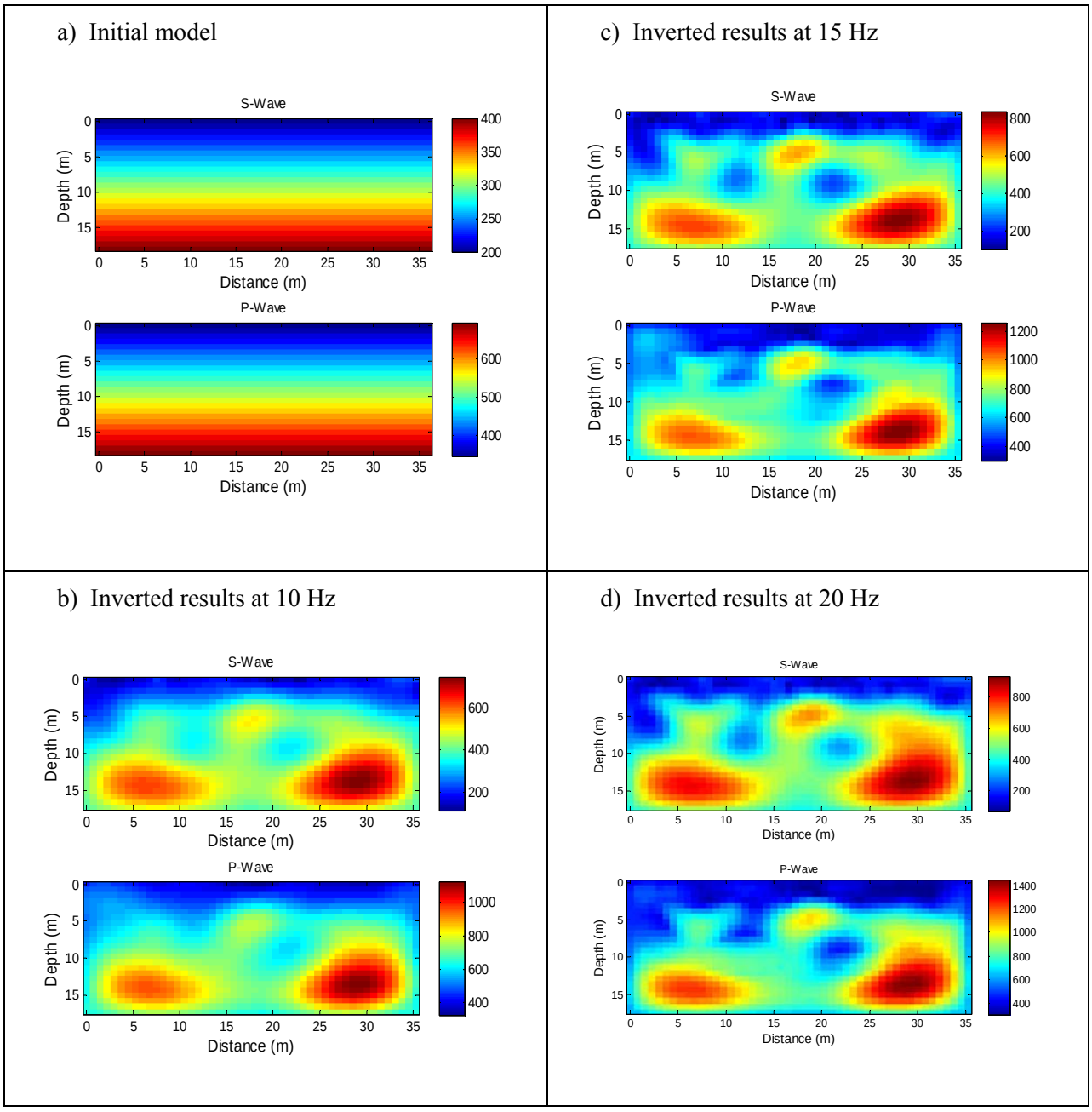


**Figure 4-11.** South Newberry site, Line 1 – G20–G140 FWI results of S-wave and P-wave velocities (m/s): a) Initial model; b) Inverted model at 10 Hz; c) Inverted model at 15 Hz; and d) Inverted model at 20 Hz.

The Poisson's ratio profile was also calculated from the independently determined S-wave and P-wave velocities (Fig. 4-10d) shown in Fig. 4-12. The computed Poisson's ratios appeared to be consistent with the soil/rock profiles. High values (0.35 to 0.50) were found for

shallow materials of silt and silty sands, and low velocity zones (blue area in Fig. 4-10d), which were possibly voids filled with raveled soil and water. Low values (0.1 to 0.2) were found for high velocity zones (red and yellow areas in Fig. 4-10d), which were dense sand and limestone.

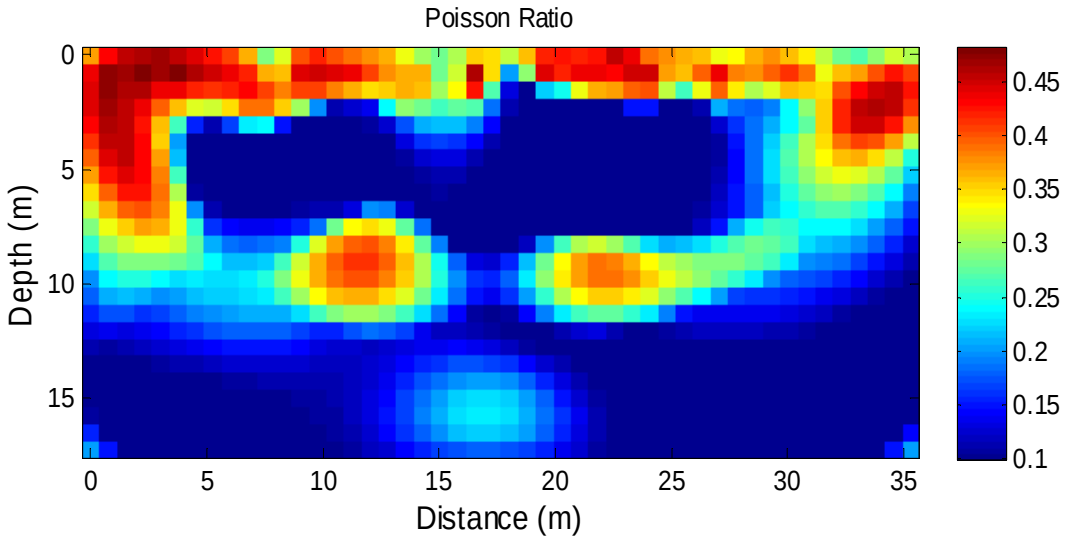


**Figure 4-12.** South Newberry site, Line 1 – G20–G140: Poisson's ratio.

### 4.3.2 Line 2 – 95A–95K

Line 2 was conducted using a linear array of twenty-four 4.5-Hz vertical geophones at a spacing of 1.2 m (4 ft) for a total receiver spread of 28 m (92 ft) [station 0.6 m to 28.6 m (2 ft to 94 ft)]. Twenty-five shots at 1.2-m spacing were recorded for a total shot spread of 29.3 m (96 ft) [station 0.0 m to 29.3m (0 to 96 ft)].

Similar to Line 1, the S-wave velocity was determined from spectral analysis of dispersion data with a range from 200 to 550 m/s (656 to 1804 ft/s). A linear increasing S-wave velocity from 200 m/s (656 ft/s) at the surface to 550 m/s (1804 ft/s) to a depth of 14.7 m (48 ft) (half of the test length) over a length of 29.3 m (96 ft) was selected. The initial P-wave velocity for the domain was calculated from the S-wave velocities assuming that the initial Poisson's ratio throughout the domain was 0.25.

Three inversion runs were performed for frequency ranges with central frequencies of 10, 15, and 20 Hz, beginning from the lowest frequency range. The medium of 14.7 m × 29.3 m (48 ft × 96 ft) was divided into 1152 cells of 0.6 m × 0.6 m (2 ft × 2 ft). During the inversion, S-wave and P-wave velocities of cells were updated independently, and each run was stopped when the observed waveform data and the estimated waveform data were similar (Fig. 4-13).

The inverted results of the three runs are shown in Figs. 4-14b, c and d for analysis of the data at 10, 15 and 20 Hz, respectively. The final inverted S-wave profile (Fig. 4-14d, top) shows a low-velocity zone at distance 20 m near Chimney 2, along with high lateral and vertical variations in limestone boundaries [S > 800 m/s (2624 ft/s)] at the bottom of profile. A valley of low-velocity area was found at distance 8 m near Chimney 3. The inverted P-wave profile (Fig. 4-14d, bottom) was consistent with the estimated S-wave profile.

The Poisson's ratio profile was calculated from the independently determined S-wave and P-wave velocities (Fig. 4-14d) and are shown in Fig. 4-15. Again, the computed Poisson's ratio appeared consistent with soil/rock profiles. High values (0.35 to 0.50) were found for shallow materials of silt and silty sands, and low velocity zones (blue area in Fig. 4-14d), which were possibly voids filled with raveled soil and water. Low values (0.1 to 0.2) were found for high velocity zones (red and yellow areas in Fig. 4-14d), which were dense sand and limestone.

For further verification of the inverted profiles, S-wave velocity profiles from two different perpendicular lines that intersected are shown in Fig. 4-16. The intersection was at distance 22.5 m (75 ft, from grid 20 ft to grid 95 ft) of Line 1 and distance 18 m (60 ft, from grid A to grid G) of Line 2. The similarity of two independent S-wave profiles suggested consistency and credibility of the FWI.

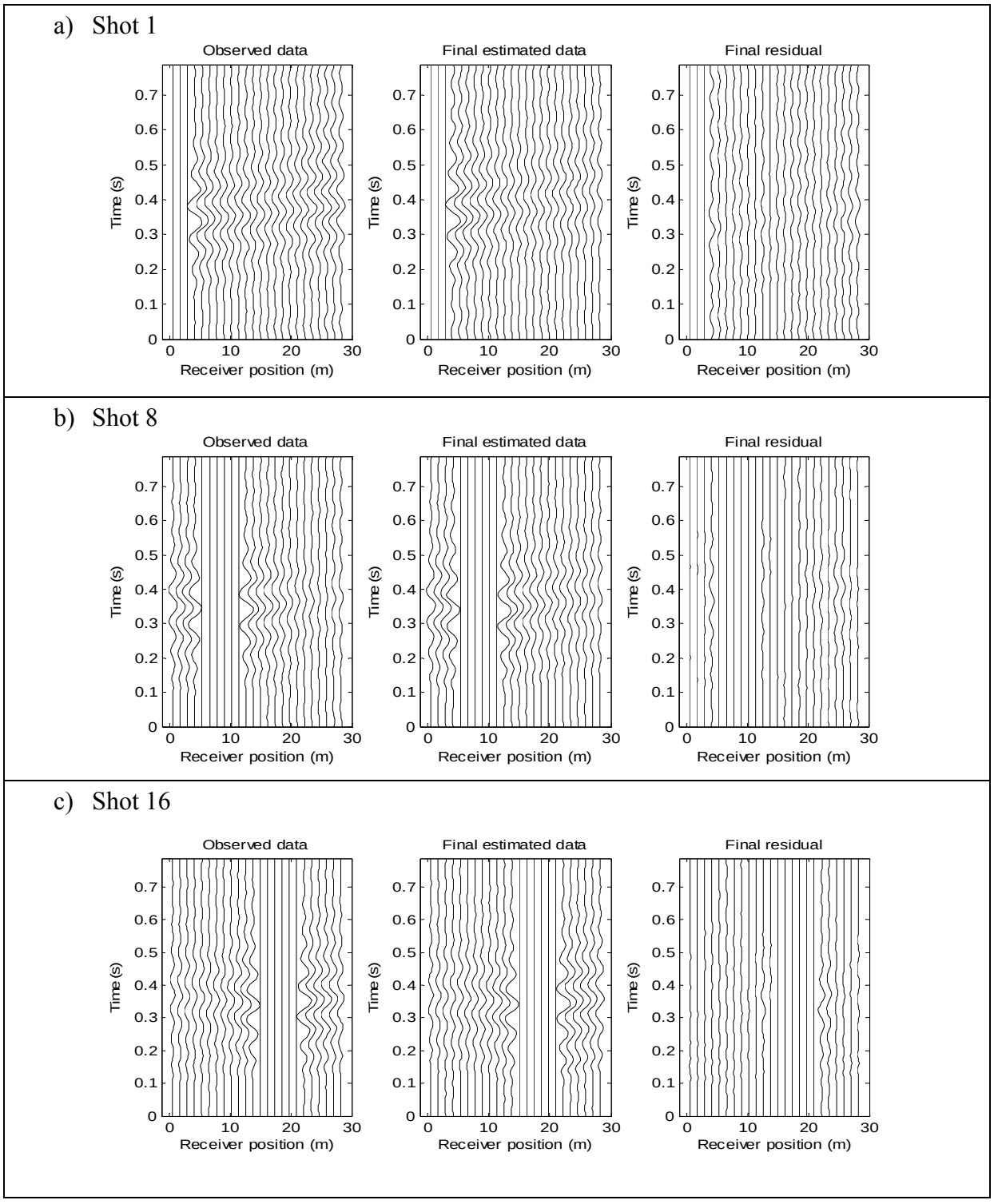


**Figure 4-13.** South Newberry site, Line 2 – 95A–95J: Comparison between observed and estimated data for a) Shot 1; b) Shot 8; and c) Shot 16.

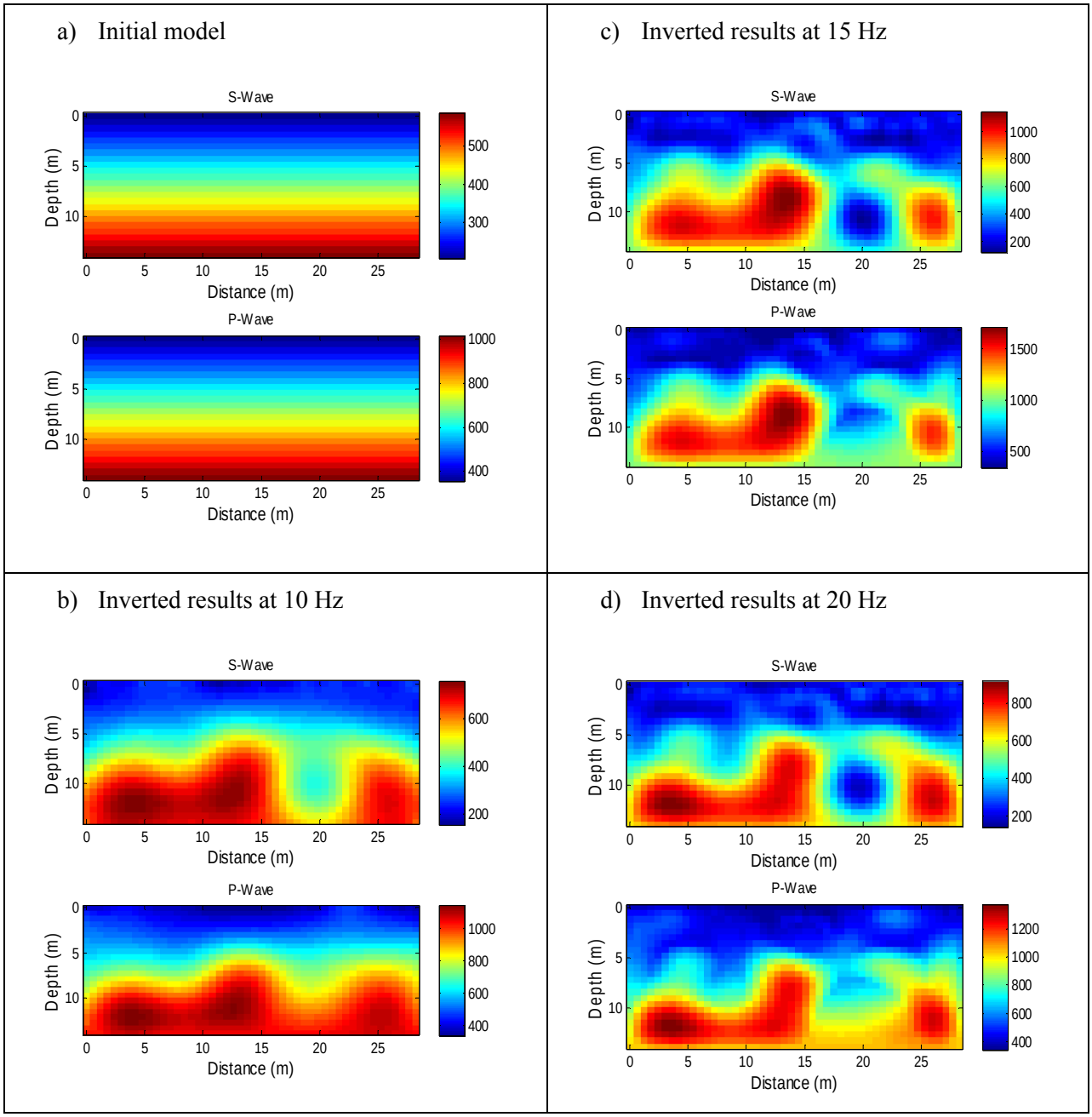


**Figure 4-14.** South Newberry site, Line 2 – 95A–95K FWI results of S-wave and P-wave velocities (m/s): a) Initial model; b) Inverted model at 10 Hz; c) Inverted model at 15 Hz; and d) Inverted model at 20 Hz.

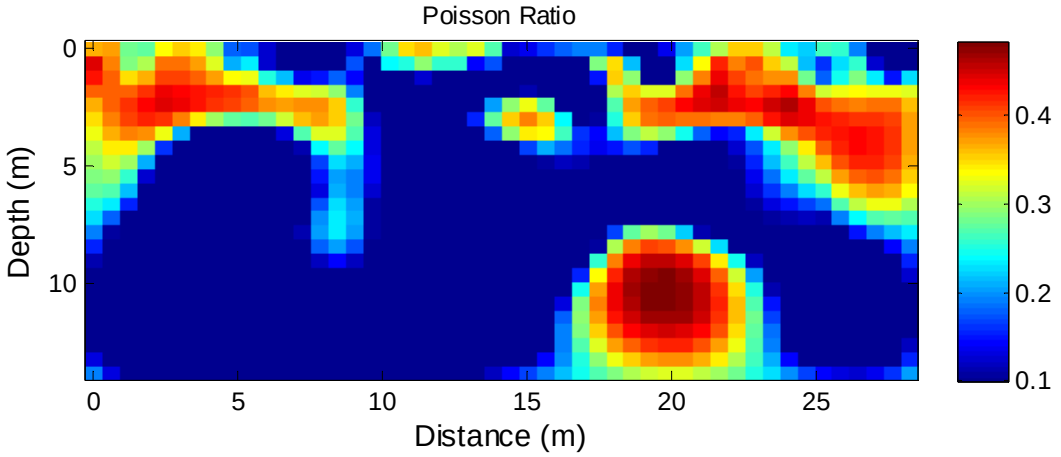


**Figure 4-15.** South Newberry site, Line 2 – 95A–95K: Poisson's ratio.

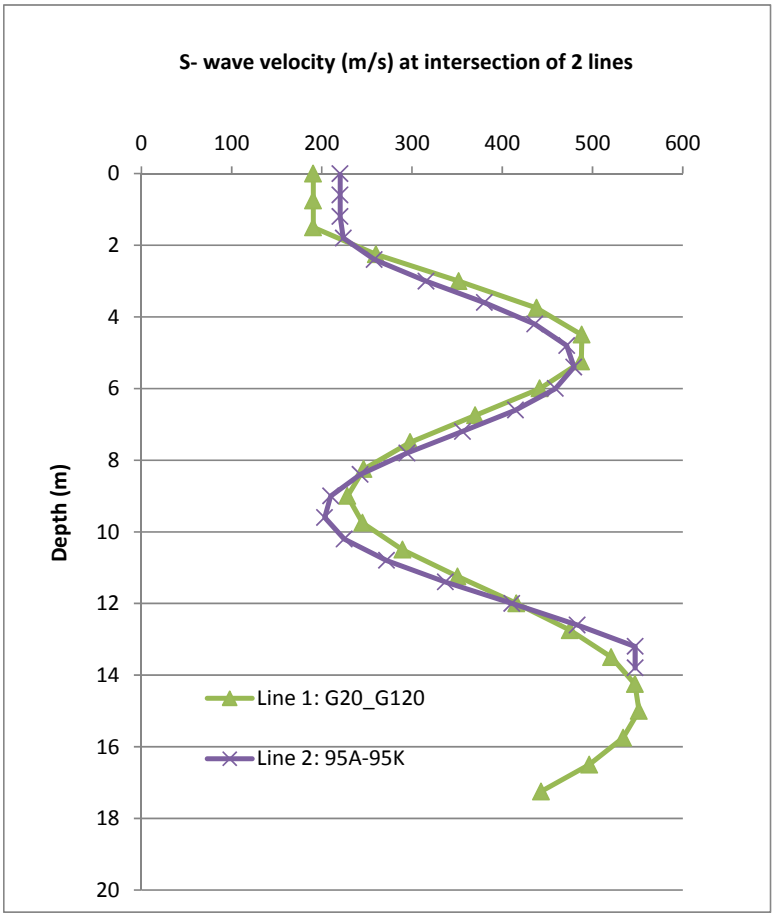


**Figure 4-16.** South Newberry site: Comparison of inverted S-wave velocity at the intersection of two lines (distance 22.5 m (75 ft) of Line 1 and distance 18 m (60 ft) of Line 2.

### 4.4 North Newberry Test Site with an Unknown Embedded Void

The final FWI data sets collected and analyzed represented the northern portion of the Newberry site which involved the random detection of a naturally occurring embedded void, or sinkhole. As this portion of the site was an open and flat area with no indication of a void (e.g., depression) on the ground surface, ten test lines were conducted along lines: K, L, M, N, O, P, Q, R, S, and T. Each line was conducted using a linear array of twenty-four 4.5-Hz vertical geophones at a spacing of 1.5 m (5 ft) for a total receiver spread of 34.5 m (115 ft) [station 0.75 m to 35.25 m (2.5 ft to 117.5 ft)]. The seismic energy was created by vertically striking a 150-mm (6 inch) square metal plate with a 90 N (20 lb) sledgehammer. Twenty-five shots at 1.5 m (5 ft) spacing were recorded for a total shot spread of 36.0 m (120 ft) [station 0.0 m to 36.0 m (0 to 120 ft)]. The seismic data from each line was analyzed with the FWI algorithm, and one line, Q, was found to have an embedded void, which is discussed here in further detail.

For the full inversion of seismic data, the initial velocity profile with depth was again established via a spectral analysis. Figure 4-17a presents a normalized power spectrum obtained using the cylindrical beamformer technique for the measured data from the shot at station 0 m (Fig. 4-17b). Rayleigh wave velocities were found to vary from 200 (656 ft/s) to about 500 m/s (1640 ft/s). Thus, the S-wave velocity, which was slightly faster than the velocity of Rayleigh wave, was assumed to range from 200 to 550 m/s (656 to 1804 ft/s). A linear increasing S-wave velocity from 200 m/s (656 ft/s) at the surface to 550 m/s (1804 ft/s) to a depth of 15 m (50 ft) over a length of 36 m (120 ft) was considered. The initial P-wave velocity of the model was calculated from the S-wave velocity profile, assuming that the initial Poisson's ratio of the whole domain was 0.25. Again, the mass density of all material was kept constant at 1800 kg/m$^3$(112 lb/ft$^3$) for all inversions.

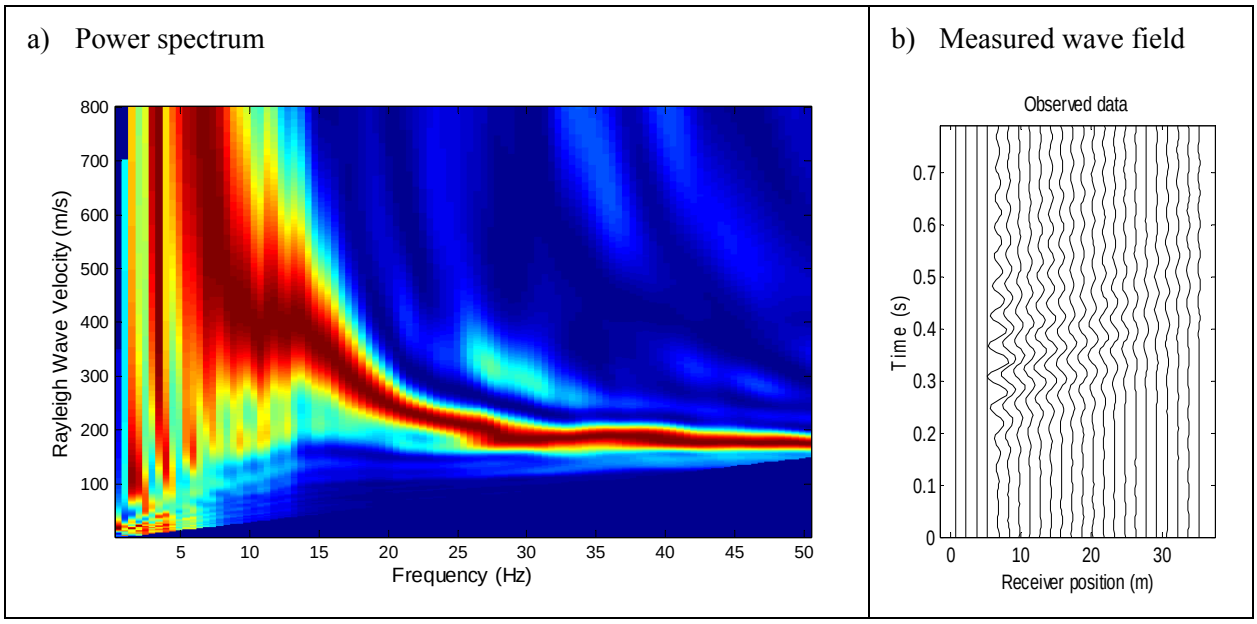


**Figure 4-17.** North Newberry site: a) Power spectrum obtained for the shot at a distance of 0 m; and b) Measured wave field.

Four separate inversions were performed for central frequencies of 6, 10, 15, and 20 Hz, beginning with the lowest frequency. For the analysis, the medium, 15 m × 36 m (50 ft × 120 ft), was divided into approximately 1000 cells, each 0.75 m × 0.75 m (2.5 ft × 2.5 ft). During the inversion, both the S-wave and P-wave velocities in each cell were updated independently, and each run was stopped after 20 iterations. Geometrical spreading corrections were implemented for the inversion. The observed waveform data, the estimated waveform data, and residuals (difference between observed and estimated) associated with the final inverted model were aligned horizontally in Fig. 4-18 for the shots at stations 12 and 36 m (40 ft and 120 ft). As evident, the observed and estimated waveform data were very similar across the entire range of offsets, and the residuals were small except at receivers near the sources, which may be attributed to near field effects.

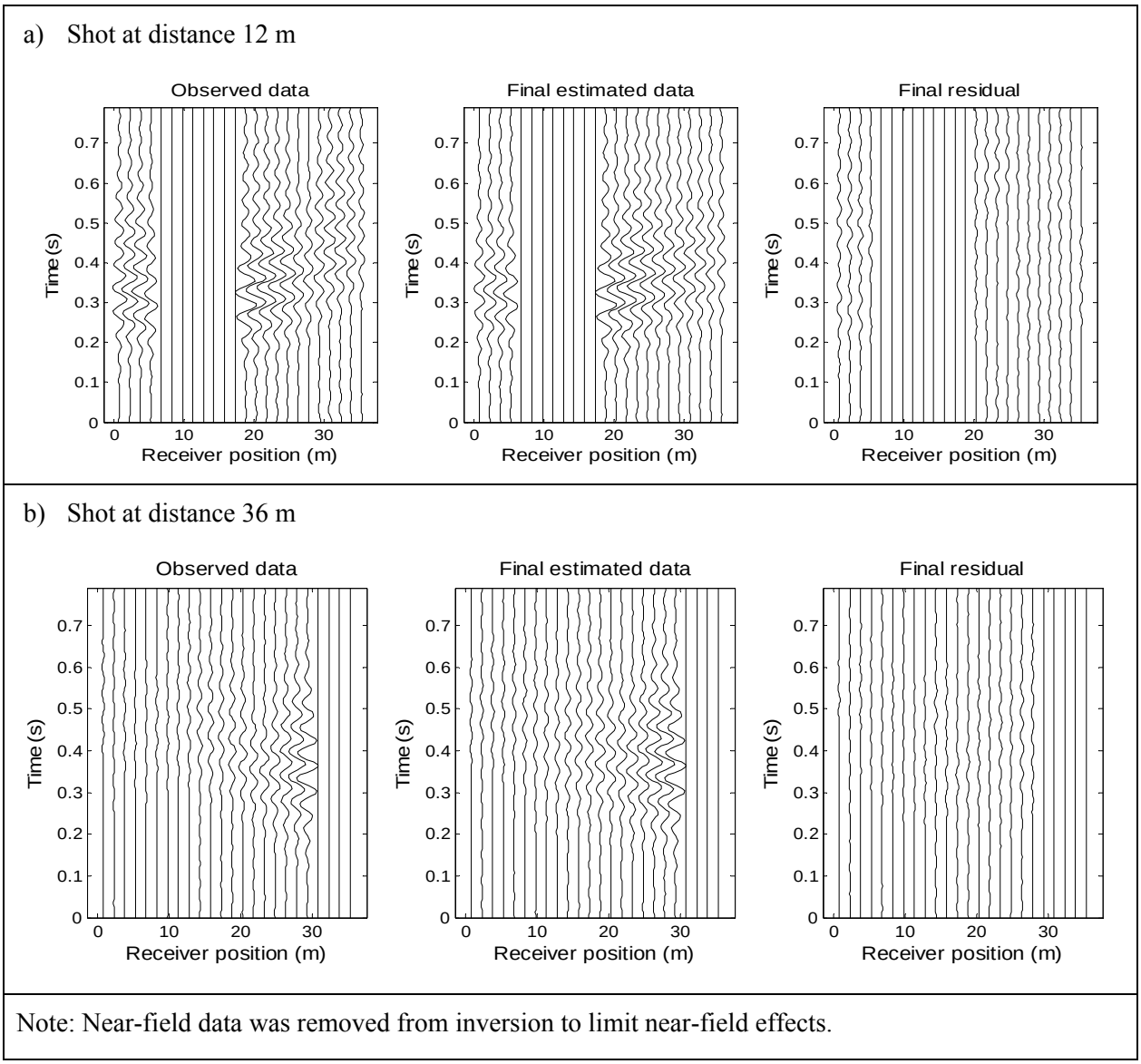


**Figure 4-18.** North Newberry site: Comparison of the observed and estimated waveforms of shots for the inversion run at the frequency range of 20 Hz at distances of: a) 12 m; and b) 36 m.

The final inversion results at 20 Hz are shown in Fig. 4-19a. The final inverted S-wave profile (top) showed a void embedded at a depth of 6 to 9 m (20 to 30 ft) [S-wave velocity less than 50 m/s (164 ft/s)], along with high lateral and vertical variations in weathered limestone [S-wave velocity > 600 m/s (2000 ft/s)] boundaries. The independently inverted P-wave profile (bottom figure) was consistent with the S-wave profile, as well as location of the void. Note, due

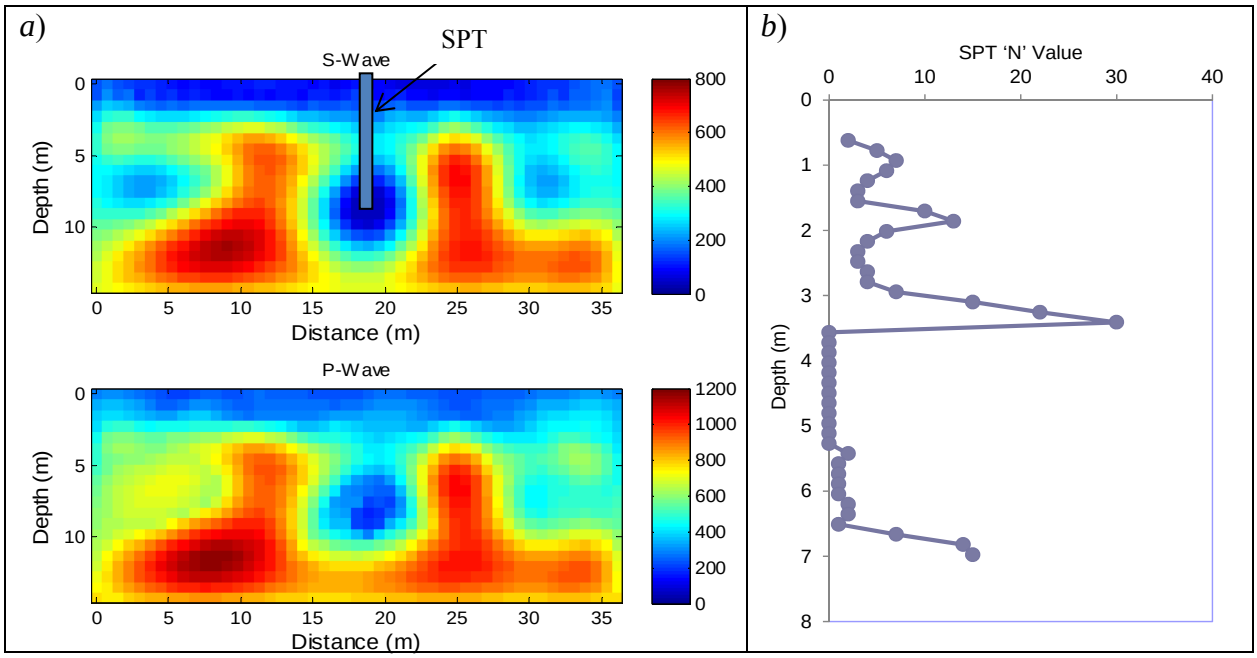


**Figure 4-19.** North Newberry site in situ test results: a) Velocity fields (m/s) of S-wave and P-wave; and b) SPT 'N' value.

to weathering, pinnacle rock surface, i.e., karst limestone, and voids are prevalent in many counties in Florida, e.g., Hillsborough, Marion, Alachua, etc.

To verify the seismic test results, a standard penetration test (SPT) was conducted at the predicted void location (distance 18 m) by the State Materials Office three weeks after the seismic test, and the SPN 'N' values are shown in Fig. 4-19b. The drilling log showed a loss of recirculation fluid at 5 m, i.e., presence of void. However, from the SPT N values, N = 0, suggested that the void occurred at 4- to 7-m depth (13 to 23 ft) and that it was possibly a sinkhole chimney or a void filled by raveled soil. The 2-D FWI proved useful in locating the void, but identified the depth [6 to 9 m (20-30 ft)] to be deeper than the real depth of the void [4 to 7 m (13-23 ft)]. This difference was mostly attributed to the discrepancy between the estimated waveform data (plane strain) versus the measured data (3-D).

The Poisson's ratio profile was also subsequently calculated from the independently determined S-wave and P-wave velocities (Fig. 4-19a) and shown in Fig. 4-20. The computed Poisson's ratio was consistent with the soil/rock profile. High values (0.35 to 0.50) were found for a shallow layer of fine sand and silt, low velocity zones, and a void that was might be filled by ravel sand, silt and water. Low values (0.1 to 0.15) were found for the limestone (red area in Fig. 4-19a).

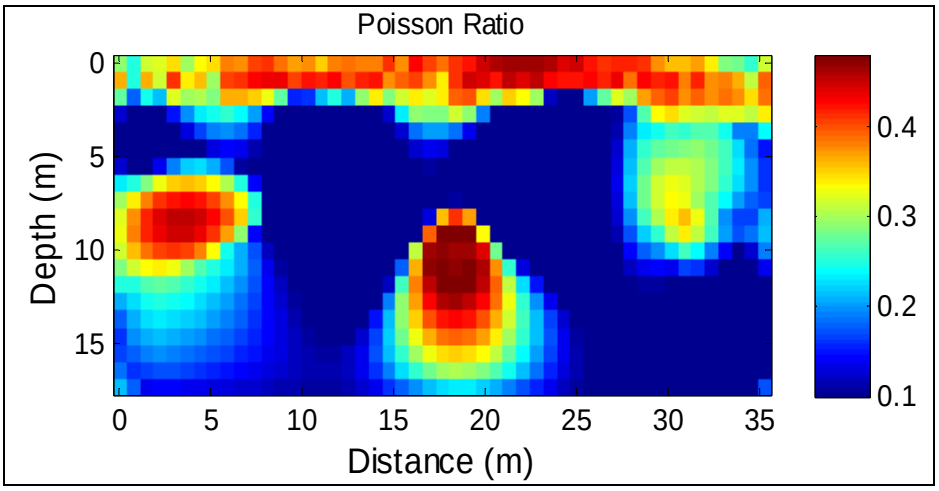


**Figure 4-20.** North Newberry site in situ test results: Poisson's ratio.

# CHAPTER 5
# CONCLUSIONS AND RECOMMENDATIONS

## 5.1 Conclusions

A new full waveform inversion algorithm for full seismic elastic waveforms was presented for identification of soil and rock layering, as well as detection of embedded voids or anomalies. The FWI technique was based on a finite-difference solution of 2-D elastic wave equations in time domain and a Gauss–Newton method to invert the seismic full wave fields of near-surface velocity profiles by matching the observed (geophones) and computed waveforms (particle velocity) on the ground surface. Virtual sources and reciprocity were used in the inversion [Gauss–Newton] to reduce the computer time. Additionally, the measured and estimated wave fields were convolved with appropriate reference traces to remove the influence of source signatures. Finally, 3-D effects were minimized by converting the point sources (sledgehammer) to line sources to improve signal matching.

The new FWI algorithm was first applied to synthetic data, i.e., a heterogeneous domain (i.e., soil layering, rock and anomalies – void filled with air or water). Also, a known velocity (S and P) profile, (i.e., layering, voids, etc.) was subject to multiple line source loads and the predicted (forward modeling) surface particle velocities were used as input to the FWI inversion algorithm. For the inversion, a simple liner velocity profile for the domain (i.e., no characterization of voids, etc.) was assumed. Comparison between inverted profile and profile used to generate the surface data showed: 1) presence of voids (air- or water-filled) was detectable with seismic full wave form inversions; 2) independent assessment of S and P velocity profiles in complex domains (i.e., layering, voids, etc.) was possible; and 3) simple linear velocity profiles

(S and P) might be used as initial conditions in the full wave form analysis, if low frequencies (e.g., 5 Hz) were used to start the inversion.

Next, the algorithm was applied to recorded field data on three separate sites in Florida: 1) buried storm sewer (i.e., known location and dimension) on UF campus; 2) recently filled sinkhole on US-441 in Marion County; and 3) FDOT retention pond in Newberry Florida. For three of the investigations with anomalies (storm sewer; sinkhole on US 441; and open chimneys in Newberry), the FWI inversion did a good job in detecting the anomalies in both the S and P velocity profiles. Moreover, the algorithm was able to detect air void (storm sewer) and void filled with water (Newberry). In addition, due to separate inversion (S- and P-wave), the algorithm was capable of computing the Poisson's ratio of the domain's materials which assisted in identifying soil (cohesionless and cohesive), rock- and void-filled with water or air.

The final set of inversions investigated on the Newberry Florida site (10 lines) had no visible surface openings or subsidence. Of interest was the location of an anomaly which was potentially a future sinkhole. Analysis of one of the lines revealed a void (water-filled) from 6 m to 9 m (20 to 30 ft). Subsequently, the SMO of FDOT performed SPT testing at the suggested anomaly, revealing loss of circulation and zero SPT 'N' values from depths of 4 m to 7 m (13 to 23 ft). The slight difference in depths was attributed to 3-D effects in the 2-D analysis.

Based on both the synthetic and field studies (three separate sites), it was concluded that full waveform inversion of surface seismic waves has tremendous potential in geotechnical surface investigation, i.e., identifying heterogeneity (layering – strong over weak, anomalies, e.g., voids). This is potentially very useful given current geotechnical invasive testing (i.e., CPT, SPT, etc.), which only identify subsurface conditions at point locations typically at spacings from 50 to 200 ft.

## 5.2 Recommendations

For the technology to be useful in general geotechnical subsurface investigation, a number of improvements or recommendations are suggested: 1) the technology (i.e., inversion software) must be self-contained; 2) be run on a laptop in the field; 3) require minimal knowledge to use; and 4) inversion must occur in 30 minutes or less (while a line of data is collected, the inversion identifies the heterogeneity of the previous line). The first and third recommendations are associated with costs (e.g., labor, i.e., technician versus PhD engineer). The second and fourth recommendations are stipulated such that only one site visit [100 m × 100 m (330 ft × 330 ft)] is required for geophysical study to assess anomalies, layering, etc. Specifically, if one line identifies an anomaly, nearby parallel or orthogonal lines may be performed based on site inversion.

Given the increase of central processing unit (CPU) speeds of laptops, and use of multiple CPUs, etc., the 30-minute inversion (e.g., four frequencies) should be viable within 18 months. To allow for general use (i.e., technician), it is recommended that the initial velocity profile (i.e., S and P) be determined automatically by the software. The latter is readily done by using the normalized power spectrum from the cylindrical beamformer technique (Tran and Hiltunen, 2008) to assess S-wave velocity profile, and assess P-wave velocity profile with an assumed Poisson ratio (e.g., 0.25). Using the latter, the only required input would be the recorded geophone spacing and recorded surface particle velocities.

REFERENCES

Brenders, A. J., and Pratt, R. G. (2007). Full waveform tomography for lithospheric imaging: Results from a blind test in a realistic crustal model, *Geophysical Journal International*, 168(1): 133–151.

Bristow, C., and Jol, H. (2003). *Ground Penetrating Radar in Sediments*, Geological Society Special Publications, London.

Cercato, M. (2011). Global surface wave inversion with model constraints, *Geophysical Prospecting*, 59: 210–226.

Cheong, S., Pyun, S., and Shin, C. (2006). Two efficient steepest-descent algorithms for source signature-free waveform inversion, *Journal of Seismic Exploration*, 14: 335–348.

Choi, Y., and Alkhalifah, T. (2011). Source-independent time-domain waveform inversion using convolved wavefields: Application to the encoded multisource waveform inversion: *Geophysics*, 76(5): R125–R134.

Clayton, R., and Engquist, B. (1977). Absorbing boundary condition for acoustic and elastic waves, *Bulletin of the Seismological Society of America*, 67(6): 1529–1540.

Conyers, L., and Goodman, D. (1997). *Ground-Penetrating Radar: An Introduction for Archaeologists*, AltaMira Press.

Daniels, D. J. (2004). *Ground Penetrating Radar, 2nd ed.*, Institution of Engineering and Technology.

Gélis, C., Virieux, J., and Grandjean, G. (2007). Two-dimensional elastic waveform inversion using Born and Rytov formulations in the frequency domain, *Geophysical Journal International*, 168: 605–633.

Hansen, R. O. (2001). Gravity and magnetic methods at the turn of the millennium, *Geophysics*, 66: 36–37.

Jol, H. M. (2009). *Ground Penetrating Radar Theory and Applications*, Elsevier Science.

Klammler, H., McVay, M., Horhota, D., and Lai, P. (2010). Influence of Spatially Variable Side Friction on Single Drilled Shaft Resistance and LRFD Resistance Factors, *Journal of Geotechnical and Geoenvironmental Engineering*, 136 (8): 1114–1123.

LaFehr, T. R. (1980). History of geophysical exploration - Gravity method, *Geophysics*, 45: 1634–1639.

Loke, M. H. (2000a). Electrical imaging surveys for environmental and engineering studies: A practical guide to 2D and 3D surveys. Unpublished short training course lecture notes. Geotomo Software, Penang, Malaysia, 65 p.

Loke, M. H. (2000b). *Res2dinv Software User's Manual, Version 3.44*. Geotomo Software, Penang, Malaysia, 86 p.

Louie, J. N. (2001). Faster, better, shear-wave velocity to 100 meters depth from refraction microtremor arrays, *Bulletin of Seismological Society of America*, 91(2): 347–364.

Nasseri–Moghaddama, A., Cascante, G., Phillips, C., and Hutchinson, D. J. (2007). Effects of underground cavities on Rayleigh waves—Field and numerical experiments, *Soil Dynamics and Earthquake Engineering*, 27: 300–313.

Nazarian, S. (1984). In situ determination of elastic moduli of soil deposits and pavement systems by spectral-analysis-of-surface-waves method. Ph.D. Dissertation. The University of Texas at Austin.

Park, C. B., Miller, R. D., and Xia, J. (1999). Multi-channel analysis of surface wave (MASW), *Geophysics*, 64(3): 800–808.

Paterson, R. J., and Reeves, C. V. (1985). Applications of gravity and magnetic surveys: The state of the art in 1985, *Geophysics*, 50: 2558–2594.

Pica, A., Diet, J. P., and Tarantola, A. (1990). Nonlinear inversion of seismic reflection data in a laterally invariant medium, *Geophysics*, 55: 84–292.

Plessix, R. E. (2008). Introduction: Towards a full waveform inversion, *Geophysical Prospecting*, 56: 761–763.

Ravaut, C., Operto, S., Improta, L., Virieux, J., Herrero, A., and Dell'Aversana, P. (2004). Multiscale imaging of complex structures from multifold wide-aperture seismic data by frequency-domain full-wavefield tomography: Application to a thrust belt, *Geophysical Journal International*, 159: 1032–1056.

Richart, F. E., Hall, J. R., and Woods, R. D. (1970). *Vibrations of Soils and Foundations*, Prentice-Hall, Inc., Englewood Cliffs, New Jersey.

Romdhane, A., Grandjean, G., Brossier, R., Rejiba, F., Operto, S., and Virieux, J. (2011). Shallow-structure characterization by 2D elastic full-waveform inversion, *Geophysics*, 76(3): R81–R93.

Schäfer, M., Groos, L., Forbriger, T., and Bohlen, T. (2012). On the effects of geometrical spreading corrections for a 2D full waveform inversion of recorded shallow seismic surface waves, 74th EAGE Conference and Exhibition, SPE EUROPEC 2012, Copenhagen, Denmark, 4-7 June.

Sheehan, J. R., Doll, W. E., and Mandell, W. A. (2005). An evaluation of methods and available software for seismic refraction tomography analysis, *Journal of Environmental and Engineering Geophysics*, 10(1): 21–34.

Sheen, D. H., Tuncay, K., Baag, C. E., and Ortoleva, P. J. (2006). Time domain Gauss–Newton seismic waveform inversion in elastic media, *Geophysical Journal International*, 167: 1373–1384.

Shipp, R. M., and Singh, S. C. (2002). Two-dimensional full wavefield inversion of wide-aperture marine seismic streamer data, *Geophysical Journal International*, 151: 325–344.

Slob, E., Sato, M., and Olhoeft, G. (2010). Surface and borehole ground-penetrating-radar developments, *Geophysics*, 75: A103–20.

Tarantola, A. (1987). *Inverse Problem Theory: Methods for Data Fitting and Parameter Estimations*, Elsevier Science Publishing Co., New York.

Tran, K. T., and Hiltunen, D. R. (2008). A comparison of shear wave velocity profiles from SASW, MASW, and ReMi techniques, *Geotechnical Earthquake Engineering and Soil Dynamics IV*, Geotechnical Special Publication, 181.

Tran, K. T., and Hiltunen, D. R. (2011). Inversion of first-arrival time using simulated annealing, *Journal of Environmental and Engineering Geophysics*, 16: 25–35.

Tran, K. T., and Hiltunen, D. R. (2012a). Inversion of combined surface and borehole first-arrival time, *Journal of Geotechnical and Geoenvironmental Engineering*, 138(3): 272–280.

Tran, K. T., and Hiltunen, D. R. (2012b). Two-dimensional inversion of full waveform using simulated annealing, *Journal of Geotechnical and Geoenvironmental Engineering*, 138(9): 1075-1090.

Tran, K. T., and Hiltunen, D. R. (2012c). One-dimensional inversion of full waveform using genetic algorithm, *Journal of Environmental and Engineering Geophysics*, 17: 197–213.

Tran, K. T., and McVay, M. (2012). Site characterization using Gauss–Newton inversion of 2-D full seismic waveform in time domain, *Soil Dynamics and Earthquake Engineering*, 43: 16–24.

Virieux, J. (1984). SH wave propagation in heterogeneous media: Velocity-stress finite-difference method, *Geophysics*, 51: 889–901.

Virieux, J. (1986). P–SV wave propagation in heterogeneous media: Velocity–stress finite-difference method, *Geophysics*, 51(4): 889–901.

Virieux, J., and Operto, S. (2009). An overview of full-waveform inversion in exploration geophysics, *Geophysics*, 74(6): WCC1–WCC26.

Wightman, W., Jalinoos, F., Sirles, P., and Hanna, K. (2003). *Applications of Geophysical Methods to Related Highway Problems*, Federal Highway Administration (FHWA), Technical manual.